

Unified discontinuous Galerkin analysis of a thermo/poro-viscoelasticity model

Stefano Bonetti¹ and Mattia Corti¹

¹*MOX-Dipartimento di Matematica, Politecnico di Milano, Piazza Leonardo da Vinci 32, Milan, 20133, Italy*

We present and analyze a discontinuous Galerkin method for the numerical modeling of a Kelvin-Voigt thermo/poro-viscoelastic problem. We present the derivation of the model, and we develop a stability analysis in the continuous setting that holds both for the full inertial and quasi-static problems and that is robust with respect to most of the physical parameters of the problem. For spatial discretization, we propose an arbitrary-order weighted symmetric interior penalty scheme that supports general polytopal grids and is robust with respect to strong heterogeneities in the model coefficients. For the semi-discrete problem, we prove the extension of the stability result demonstrated in the continuous setting. A wide set of numerical simulations is presented to assess the convergence and robustness properties of the proposed method. Moreover, we test the scheme with literature and physically sound test cases for *proof-of-concept* applications in the geophysical context.

1 Introduction

In recent years, there has been an increasing interest in studying the poroelasticity equations [16, 20, 45, 53, 54, 63]. The equations of linear poroelasticity are commonly known as Biot's equations, and they find origin in the works of Biot [12] and Terzaghi [62]. This model aims to study and describe the interaction between the fluid flow and elastic deformation within a porous media. This problem was initially associated with geophysical applications, where the subsoil is modeled as a fully saturated poroelastic material (examples of application can be found, e.g., in [29, 35, 55]). Through the years, the classical poroelastic equations have been enhanced to couple them with other physical phenomena by including quantities that may influence (and may be influenced by) the fluid flow and the elastic deformation. Some examples can be found in poroelasto-acoustic coupling [2], which finds application in the context of the earthquake, and in the thermo-poroelasticity theory [23, 24], which is used for modeling geothermal energy production procedures and greenhouse gas sequestration.

A growing interest in the poroelasticity field has been motivated by its application to biological tissues. Indeed, organs, bones, and engineered tissue scaffolds can be modeled starting from the poroelasticity theory [14, 15, 46]. Interesting results in the biological modeling, for example, in the brain context, can be obtained using the linear poroelasticity model [30]. More sophisticated multiple-network poroelastic theory [32] considers multiple fluid compartments and, consequently, coupling terms coming from the interaction between different fluids.

However, biological tissues typically exhibit both elastic and viscoelastic behavior due to the combined action of elastin and collagen [48]. Linear viscoelastic effects can be incorporated into traditional linear Biot dynamics by considering the viscoelastic strain and possibly adjusting the formula for the local fluid content accordingly (depending on the specific scenario considered, either focusing on incompressible or compressible constituents). Some early works on poro-viscoelastic solids and their modeling are [33, 56]. This work considers the simplest (linear) visco-elasticity inclusion: the Kelvin-Voigt type [13, 17]. We remark that the viscoelastic effects may be of interest also for geophysical applications. Indeed, traditionally, they were considered in the displacement dynamics by invoking the so-called secondary consolidation [42, 49], for instance, for studies on clays.

This paper uses the full inertial Biot’s system for describing poro-viscoelasticity, which is formally equivalent to thermoelasticity and thermo-viscoelasticity problems [58]. Fully-dynamic thermoelasticity can be used in the context of earthquake modeling. Indeed, a mechanical source of elastic waves induces a temperature field whose heat flow equalizes the temperature difference with the surroundings, giving rise to energy dissipation. On the other hand, a heat source generates elastic or viscoelastic waves [28]. Some *proof-of-concept* numerical results in the direction of thermoelasticity are presented in this paper. Including viscous effects in the thermoelasticity theory may be useful for describing the behavior of the elastomers under large strains [22].

This paper aims to provide a general and unified framework for studying thermo/poro-viscoelasticity problems in both their quasi-static and dynamic forms (i.e., considering inertial terms). Specifically, the treatment of the model problem highlights which terms are more or less significant depending on the values of the physical parameters and, consequently, on the reference application. Second, the stability analysis of the problem is developed to have only weak constraints on the model parameters; in particular, it is designed to be robust to the presence of the inertial terms within the two equations and the parameters describing the viscoelasticity characteristics in the model problem.

For the spatial discretization of the problem, we adopt a discontinuous Galerkin finite element method on polytopal grids (PolyDG) [1, 25]. The PolyDG schemes are appealing because of their geometrical flexibility, facilitating local mesh refinement and coarsening. Moreover, they allow us to efficiently handle highly heterogeneous media by better representing inner discontinuities. Geometrical flexibility is a desirable feature in both the geophysical and biological contexts, where discretization should capture peculiar features of the domain without dramatically affecting the number of elements. Another advantage of polytopal discretization techniques is the possibility of exploiting arbitrary- and, in particular, high-order approximations. In second-order hyperbolic problems, high-order discretizations minimize the dispersion and diffusive phenomena. However, we remark that for subsurface applications, we may not have the regularity needed to justify high-order discretizations due to the large variabilities of the model’s coefficients [39, 60]. The proposed method’s arbitrary-order accuracy, combined with its geometric flexibility, allows using *hp*-refinement techniques, taking full advantage of agglomeration techniques and reducing the overall computational cost.

Examples of PolyDG schemes can be found in [2] for poroelasticity, in [4, 18, 19] for thermo-hydro-mechanics (both in the quasi-static and fully-dynamic regimes), and in [32] for multiple-network poroelasticity. Moreover, in [2, 3, 34], PolyDG methods for wave propagation problems in porous media are analyzed. Last, in [9], a discontinuous Galerkin method for the Kelvin-Voigt viscoelastic fluid model is proposed. In the literature, other discretization strategies for the poroelasticity problems include, e.g., finite Volume methods [11, 57], Hybrid Finite Volume method [8], Hybrid High-Order [21], Hybridizable Discontinuous Galerkin [40], lowest order Raviart-Thomas coupled with conforming finite element methods [20], and eXtended finite element method [44].

The major highlights of this paper are: (a) a detailed discussion of the model problem, in which the importance of the inertial terms as a function of the physical parameters of the problem is highlighted; (b) an analysis covering both the static problem case and the fully inertial problem that investigates the stability of the problem under mild assumptions on the problem coefficients and (c) a wide set of numerical simulations that are intended to prove the convergence and robustness properties of the method, test the method against literature benchmarks, and explore the applicability of the method in *physically-sound* test cases.

The rest of the paper is organized as follows: the model problem, its derivation, and its weak formulation are reported in Section 2. In Section 3, we prove the stability of the continuous problem. In Section 4, we design the discretization of the problem. In particular, in Section 4.2, we detail the PolyDG space discretization, and in Section 4.3, we show the time-discretization techniques we exploit for the hyperbolic-hyperbolic case and the hyperbolic-parabolic case. Moreover, we extend the stability result obtained in Section 3 for the discrete setting. Last, we report numerical results in Section 5. Namely, we start by assessing the method’s performance in terms of convergence properties and robustness, and then we address benchmark and physically sound test cases.

2 Model problem

Let $\Omega \subset \mathbb{R}^d$, $d = \{2; 3\}$, be an open, polygonal/polyhedral domain with Lipschitz boundary $\partial\Omega$. Given a final time $T_f > 0$, the problem reads: *find* (\mathbf{u}, φ) *such that*:

$$\begin{cases} \rho \ddot{\mathbf{u}} - \nabla \cdot \boldsymbol{\sigma}(\mathbf{u}, \dot{\mathbf{u}}, \varphi) = \mathbf{f} & \text{in } \Omega \times (0, T_f], \\ d_0 (\dot{\varphi} + \tau_1 \ddot{\varphi}) + \gamma (\nabla \cdot \dot{\mathbf{u}} + \tau_2 \nabla \cdot \ddot{\mathbf{u}}) - \nabla \cdot (\mathbf{D} \nabla \varphi) = g & \text{in } \Omega \times (0, T_f], \end{cases} \quad (1a) \quad (1b)$$

where the unknowns (\mathbf{u}, φ) stand for the solid displacement and a generalized pressure variable. In problem (1), equation (1a) represents the momentum conservation law. At the same time, equation (1b) can represent both a mass conservation or an energy conservation law based on the physical interpretation given to the variable φ , which we discuss later in this section. Thus, the terms \mathbf{f} and g are source terms that represent a body force and a mass or energy source, respectively. Finally, problem (1) is supplemented by imposing suitable boundary and initial conditions.

In (1) and in the rest of the article, we use the short-hand notation $\dot{\psi}$ and $\ddot{\psi}$ for denoting the first and second partial derivatives with respect to time of a function $\psi : \Omega \times (0, T_f] \rightarrow \mathbb{R}$, respectively.

The constitutive law for the total stress tensor $\boldsymbol{\sigma}$ is obtained as in [33] under the small deformations assumption, taking into account the isotropic effect of the generalized-pressure field on the porous matrix:

$$\boldsymbol{\sigma}(\mathbf{u}, \dot{\mathbf{u}}, \varphi) = 2\mu\boldsymbol{\epsilon}(\mathbf{u}) + 2\mu\delta_1\boldsymbol{\epsilon}(\dot{\mathbf{u}}) + (\lambda\nabla \cdot \mathbf{u} + \lambda\delta_2\nabla \cdot \dot{\mathbf{u}} + \gamma\varphi)\mathbf{I},$$

where \mathbf{I} is the identity tensor and $\boldsymbol{\epsilon}(\mathbf{u}) = \frac{1}{2}(\nabla\mathbf{u} + \nabla\mathbf{u}^T)$ is the strain tensor. Moreover, the dependency on the velocity of the deformation \mathbf{u} models the secondary consolidation phenomena in poroelasticity for coil applications [10].

The generalized pressure variable φ can be considered a pressure in a poro-(visco)elasticity framework or a temperature in a thermo-(visco)elasticity one. In the first case, the second equation rises from the linearized equation of mass conservation [33]:

$$d_0\dot{\varphi} + \gamma(\nabla \cdot \dot{\mathbf{u}}) + \nabla \cdot \mathbf{w} = \tilde{g},$$

where \mathbf{w} is the filtration velocity, d_0 is the specific storage coefficient, and γ is the Biot-Willis parameter [33]. Then, equation (1b) is obtained by adopting a Darcy law that considers the acceleration of the fluid [50]:

$$\frac{\rho_f}{\phi}\mathbf{K}\dot{\mathbf{w}} = -\mathbf{K}\nabla\varphi - \mathbf{w},$$

where ρ_f is the fluid density, ϕ is the porosity (the ratio between the void space in a porous medium and its whole volume such that $0 < \phi_0 \leq \phi \leq \phi_1 < 1$ [59]), \mathbf{K} is the permeability divided by the dynamic fluid viscosity and \tilde{g} is the forcing term. In particular, to obtain the formulation in equation (1b), we need to define $\tau_1 = \rho_f\mathbf{K}\phi^{-1}$, $\tau_2 = \rho_f\mathbf{K}\phi^{-1}$, $\mathbf{D} = \mathbf{K}$, $g = \tau_1\dot{\tilde{g}} + \tilde{g}$.

On the contrary, in the thermoelastic case, considering φ as a temperature, equation (1b) can be derived from the linearized equation of energy conservation [33]:

$$d_0\dot{\varphi} + \gamma(\nabla \cdot \dot{\mathbf{u}}) + \nabla \cdot \mathbf{q} = \tilde{g},$$

where \mathbf{q} is the heat flux, d_0 is the thermal dilatation coefficient, and γ is the thermal stress parameter [33]. Then, equation (1b) is obtained by adopting a Maxwell-Vernotte-Cattaneo law that considers a relaxation time in the heat conduction equation [50]:

$$\tau\dot{\mathbf{q}} = -\boldsymbol{\Theta}\nabla\varphi - \mathbf{q},$$

where τ is the relaxation time, $\boldsymbol{\Theta}$ is the effective thermal conductivity and \tilde{g} is the forcing term. In particular, to obtain the formulation in equation (1b), we need to define $\tau_1 = \tau$, $\tau_2 = \tau$, $\mathbf{D} = \boldsymbol{\Theta}$, $g = \tau_1\dot{\tilde{g}} + \tilde{g}$. In both cases, the choice of considering two different values τ_1 and τ_2 in the final model is for generalization purposes.

The coefficients appearing in (1), along with their unit of measure and physical meaning in poroelasticity or thermoelasticity frameworks, are reported in Table 1:

Parameter	Unit	Quantity
ρ_f	kg/m ³	Saturating fluid density
ρ_s	kg/m ³	Solid matrix density
ϕ	-	P : Porosity
ρ	kg m ⁻³ kg m ⁻³	P : Density $\rho = \phi\rho_f + (1 - \phi)\rho_s$ T : Density $\rho = \rho_s$
μ, λ	Pa	Lamé parameters
δ_1, δ_2	s	Viscoelasticity retardation times
γ	- Pa K ⁻¹	P : Biot–Willis constant T : Thermal stress coefficient
d_0	Pa ⁻¹ Pa K ⁻²	P : Specific storage coefficient T : Thermal capacity
D	m ² Pa ⁻¹ s ⁻¹ m ² K ⁻² s ⁻¹	P : Permeability divided by dynamic fluid viscosity T : Effective thermal conductivity
τ_1, τ_2	s s	P : Relaxation times T : Maxwell-Vernotte-Cattaneo relaxation times

Table 1: Model coefficients appearing in problem (1) with explicit indication of the associated framework of the description: poroelasticity (P) or thermoelasticity (T). Where no indication is provided, the unit and the description are valid for both frameworks.

As already mentioned, from the general formulation of equation (1) we can recover some specific models.

Poroelasticity model

The classical poroelastic Biot problem [12], can be recovered by taking the pressure field $p = \varphi$ and considering $\tau_1 = \tau_2 = \delta_1 = \delta_2 = 0$.

$$\begin{cases} \rho\ddot{\mathbf{u}} - 2\nabla \cdot (\mu\boldsymbol{\epsilon}(\mathbf{u})) + \nabla(\lambda\nabla \cdot \mathbf{u}) + \nabla(\gamma p) = \mathbf{f} & \text{in } \Omega \times (0, T_f], \\ d_0\dot{p} + \gamma(\nabla \cdot \dot{\mathbf{u}}) - \nabla \cdot (\mathbf{D}\nabla p) = g & \text{in } \Omega \times (0, T_f]. \end{cases}$$

Thermoelasticity model

The thermoelasticity problem with the Maxwell-Vernotte-Cattaneo relaxation law can be recovered by taking the temperature field $T = \varphi$ and considering $\tau_1 = \tau_2 = \tau$ and $\delta_1 = \delta_2 = 0$.

$$\begin{cases} \rho\ddot{\mathbf{u}} - 2\nabla \cdot (\mu\boldsymbol{\epsilon}(\mathbf{u})) + \nabla(\lambda\nabla \cdot \mathbf{u}) + \nabla(\gamma T) = \mathbf{f} & \text{in } \Omega \times (0, T_f], \\ d_0(\dot{T} + \tau\ddot{T}) + \gamma(\nabla \cdot \dot{\mathbf{u}} + \tau\nabla \cdot \ddot{\mathbf{u}}) - \nabla \cdot (\mathbf{D}\nabla T) = g & \text{in } \Omega \times (0, T_f]. \end{cases}$$

By taking also $\tau = 0$, we recover the formulation with the Fourier law for the temperature.

Poro-viscoelasticity model

The classical poro-viscoelasticity problem [17] can be recovered by taking the pressure field $p = \varphi$ and considering $\tau_1 = \tau_2 = 0$.

$$\begin{cases} \rho\ddot{\mathbf{u}} - \nabla \cdot (2\mu(\boldsymbol{\epsilon}(\mathbf{u}) + \delta_1\boldsymbol{\epsilon}(\dot{\mathbf{u}}))) + \nabla(\lambda(\nabla \cdot \mathbf{u} + \delta_2\nabla \cdot \dot{\mathbf{u}})) + \nabla(\gamma p) = \mathbf{f} & \text{in } \Omega \times (0, T_f], \\ d_0\dot{p} + \gamma\nabla \cdot \dot{\mathbf{u}} - \nabla \cdot (\mathbf{D}\nabla p) = g & \text{in } \Omega \times (0, T_f]. \end{cases}$$

By taking $\delta_1 = 0$, we recover the secondary consolidation poroelastic model.

2.1 Weak formulation

Before presenting the variational formulation of problem (1), we introduce the required notation. For $X \subseteq \Omega$, we denote by $L^p(X)$ the standard Lebesgue space of index $p \in [1, \infty]$ and by $H^q(X)$ the Sobolev space of index $q \geq 0$ of real-valued functions defined on X . The notation $\mathbf{L}^p(X)$ and $\mathbf{H}^q(X)$ is adopted in place of $[L^p(X)]^d$ and $[H^q(X)]^d$, respectively. These spaces are equipped with natural inner products and norms denoted by $(\cdot, \cdot)_X = (\cdot, \cdot)_{L^2(X)}$ and $\|\cdot\|_X = \|\cdot\|_{L^2(X)}$, with the convention that the subscript can be omitted in the case $X = \Omega$.

We denote by $\langle \cdot, \cdot \rangle$ the duality pairing between the space Y^* and Y ; the former being the dual space of the latter. Moreover, we denote by $\|\cdot\|_*$ the dual norm in the space Y^* .

For the sake of brevity, in what follows, we make use of the symbol $x \lesssim y$ to denote $x \leq Cy$, where C is a positive constant independent of the discretization parameters but possibly dependent on physical coefficients and final time T_f .

To derive the weak formulation of problem (1) we start by providing the definition of the functional spaces that take into account the essential boundary conditions, namely

$$V = H_0^1(\Omega) = \{\varphi \in H^1(\Omega) \text{ s.t. } \varphi|_{\partial\Omega} = 0\}, \quad \mathbf{V} = [V]^d.$$

Next, we multiply (1) times suitable test functions, integrate in space, and we get:

For any time $t \in (0, T_f]$, find $(\mathbf{u}, \varphi)(t) \in \mathbf{V} \times V$ such that:

$$\begin{aligned} \mathcal{M}_u(\ddot{\mathbf{u}}, \mathbf{v}) + (2\mu\delta_1 \boldsymbol{\epsilon}(\dot{\mathbf{u}}), \boldsymbol{\epsilon}(\mathbf{v})) + (\lambda\delta_2 \nabla \cdot \dot{\mathbf{u}}, \nabla \cdot \mathbf{v}) \\ + (2\mu\boldsymbol{\epsilon}(\mathbf{u}), \boldsymbol{\epsilon}(\mathbf{v})) + (\lambda\nabla \cdot \mathbf{u}, \nabla \cdot \mathbf{v}) - (\gamma\nabla \cdot \mathbf{v}, \varphi) = (\mathbf{f}, \mathbf{v}) \quad \forall \mathbf{v} \in \mathbf{V}, \end{aligned} \quad (2)$$

$$\mathcal{M}_{\varphi, \tau_1}(\ddot{\varphi}, \psi) + (\gamma\tau_2 \nabla \cdot \dot{\mathbf{u}}, \psi) + \mathcal{M}_{\varphi}(\dot{\varphi}, \psi) + (\gamma\nabla \cdot \dot{\mathbf{u}}, \psi) + (\mathbf{D}\nabla\varphi, \nabla\psi) = (g, \psi) \quad \forall \psi \in V,$$

where for every $(\mathbf{u}, \varphi), (\mathbf{v}, \psi) \in \mathbf{V} \times V$ we have set: $\mathcal{M}_u(\mathbf{u}, \mathbf{v}) = (\rho \mathbf{u}, \mathbf{v})$, $\mathcal{M}_{\varphi, \tau_1}(\varphi, \psi) = (d_0\tau_1 \varphi, \psi)$, and $\mathcal{M}_{\varphi}(\varphi, \psi) = (d_0 \varphi, \psi)$.

3 Stability analysis

This section is devoted to proving the stability bounds of the continuous weak solution of problem (2). Before stating the theorem, we introduce the following auxiliary norms of the displacement \mathbf{u} in \mathbf{V} :

$$\begin{aligned} \|\mathbf{u}\|_{\mathbf{V}}^2 &= 2\|\sqrt{\mu}\boldsymbol{\epsilon}(\mathbf{u})\|^2 + \|\sqrt{\lambda}\nabla \cdot \mathbf{u}\|^2, \\ \|\mathbf{u}\|_{\mathbf{V}_\delta}^2 &= 2\|\sqrt{\mu\delta_1}\boldsymbol{\epsilon}(\mathbf{u})\|^2 + \|\sqrt{\lambda\delta_2}\nabla \cdot \mathbf{u}\|^2. \end{aligned}$$

Moreover, we introduce an assumption on the regularity of model parameters:

Assumption 3.1 (Coefficients' regularity). We assume the following regularities for the coefficients and the forcing terms:

- (i) $\mu, \lambda, \rho, d_0, \gamma, \tau_1, \tau_2, \delta_1, \delta_2 \in L^\infty(\Omega)$, moreover we require $\mu > 0$;
- (ii) $\mathbf{D} \in \mathbf{L}^\infty(\Omega)$ and $\exists d > 0 \forall \boldsymbol{\xi} \in \mathbb{R}^d : d|\boldsymbol{\xi}|^2 \leq \boldsymbol{\xi}^\top \mathbf{D} \boldsymbol{\xi} \quad \forall \boldsymbol{\xi} \in \mathbb{R}^d$;
- (iii) $\mathbf{f} \in C^0(0, T_f; \mathbf{H}^{-1}(\Omega))$;
- (iv) $g \in C^0(0, T_f; H^{-1}(\Omega))$;
- (v) $\mathbf{u}_0 \in \mathbf{H}_0^1(\Omega), \dot{\mathbf{u}}_0 \in \mathbf{L}^2(\Omega), \varphi_0 \in L^2(\Omega)$, and $\dot{\varphi}_0 \in L^2(\Omega)$.

Theorem 3.1. Let us consider – for any time $t \in (0, T_f]$ – $(\mathbf{u}, \varphi)(t) \in \mathbf{V} \times V$ to be the solution of the weak problem (2) with homogeneous Dirichlet boundary conditions. Under Assumption 3.1, then the following stability estimate holds:

$$\begin{aligned} \|\sqrt{\tau_2\rho}\mathbf{u}\|^2 + \int_0^t \left(\|\tau_2\sqrt{\rho}\dot{\mathbf{u}}\|^2 + \|\sqrt{\rho}\mathbf{u}\|^2 + \left\| \frac{\tau_2}{2} \mathbf{u} \right\|_{\mathbf{V}}^2 + \|\tau_2\mathbf{u}\|_{\mathbf{V}_\delta}^2 + \|\sqrt{\tau_2\tau_1 d_0}\varphi\|^2 \right) \lesssim \\ \|\sqrt{\tau_2\rho}\mathbf{u}_0\|^2 + tI_0 + \int_0^t \left(\|\mathbf{F}\|_*^2 + \frac{\|\sqrt{\tau_2}G\|_*^2}{\|\sqrt{\mathbf{D}}\|^2} + t \left\| \frac{\tau_2\mathbf{f}}{\sqrt{\mu\delta_1}} \right\|_*^2 + t \frac{\|\tau_2g\|_*^2}{\|\sqrt{\mathbf{D}}\|^2} + t \left\| \frac{\mathbf{F}}{\sqrt{\mu\delta_1}} \right\|_*^2 + t \frac{\|G\|_*^2}{\|\sqrt{\mathbf{D}}\|^2} \right), \end{aligned}$$

where $\mathbf{F} = \int_0^t \mathbf{f}$ and $G = \int_0^t g$. Moreover, $I_0 = \|\tau_2 \sqrt{\rho} \dot{\mathbf{u}}_0\|^2 + \|\sqrt{\rho} \mathbf{u}_0\|^2 + \|\tau_2 \mathbf{u}_0\|_{\mathbf{V}}^2 + \|\sqrt{\tau_2 \tau_1 d_0} \varphi_0\|^2$. In this theorem, the (hidden) stability constant is independent of the physical parameters.

Proof. To start the proof of stability, we introduce two auxiliary variables $\Psi(t) = \int_0^t \varphi(s) ds$ and $\mathbf{W}(t) = \int_0^t \mathbf{u}(s) ds$. Then, we define two additional problems. The first is obtained by integrating Equation (1b) in time:

$$\begin{cases} \rho \dot{\mathbf{u}} - 2\nabla \cdot \mu \boldsymbol{\epsilon}(\mathbf{u}) - 2\nabla \cdot \mu \delta_1 \boldsymbol{\epsilon}(\dot{\mathbf{u}}) - \nabla(\lambda \nabla \cdot \mathbf{u}) - \nabla(\lambda \delta_2 \nabla \cdot \dot{\mathbf{u}}) + \nabla(\gamma \varphi) = \mathbf{f}, \\ d_0(\varphi + \tau_1 \dot{\varphi}) + \gamma(\nabla \cdot \mathbf{u} + \tau_2 \nabla \cdot \dot{\mathbf{u}}) - \nabla \cdot (\mathbf{D} \nabla \Psi) = G, \end{cases} \quad (3)$$

The second formulation is obtained by integrating both Equations (1a) and (1b) in time:

$$\begin{cases} \rho \dot{\mathbf{u}} - 2\nabla \cdot \mu \boldsymbol{\epsilon}(\mathbf{W}) - 2\nabla \cdot \mu \delta_1 \boldsymbol{\epsilon}(\mathbf{u}) - \nabla(\lambda \nabla \cdot \mathbf{W}) - \nabla(\lambda \delta_2 \nabla \cdot \mathbf{u}) + \nabla(\gamma \Psi) = \mathbf{F}, \\ d_0(\varphi + \tau_1 \dot{\varphi}) + \gamma(\nabla \cdot \mathbf{u} + \tau_2 \nabla \cdot \dot{\mathbf{u}}) - \nabla \cdot (\mathbf{D} \nabla \Psi) = G. \end{cases} \quad (4)$$

The first step of the proof is to test problem (3) by $(\tau_2 \dot{\mathbf{u}}, \varphi)$ and multiply everything by τ_2 . We obtain:

$$\begin{aligned} \frac{1}{2} \frac{d}{dt} \left(\|\tau_2 \sqrt{\rho} \dot{\mathbf{u}}\|^2 + \|\tau_2 \mathbf{u}\|_{\mathbf{V}}^2 + \|\sqrt{\tau_2 \tau_1 d_0} \varphi\|^2 + \|\sqrt{\tau_2 \mathbf{D}} \nabla \Psi\|^2 \right) + \|\tau_2 \dot{\mathbf{u}}\|_{\mathbf{V}_\delta}^2 + \|\sqrt{\tau_2 d_0} \varphi\|^2 \\ = -(\gamma \tau_2 \nabla \cdot \mathbf{u}, \varphi) + (\tau_2^2 \mathbf{f}, \dot{\mathbf{u}}) + (\tau_2 G, \varphi) \end{aligned}$$

The second step of the proof is to test problem (4) by (\mathbf{u}, Ψ) and we get:

$$\begin{aligned} \frac{1}{2} \frac{d}{dt} \left(\|\sqrt{\rho} \mathbf{u}\|^2 + \|\mathbf{W}\|_{\mathbf{V}}^2 + \|\sqrt{d_0} \Psi\|^2 \right) + \|\mathbf{u}\|_{\mathbf{V}_\delta}^2 + \|\sqrt{\mathbf{D}} \nabla \Psi\|^2 \\ = (\gamma \tau_2 \nabla \cdot \mathbf{u}, \varphi) - \frac{d}{dt} (\gamma \tau_2 \nabla \cdot \mathbf{u}, \Psi) - (d_0 \tau_1 \dot{\varphi}, \Psi) + (\mathbf{F}, \mathbf{u}) + (G, \Psi) \end{aligned}$$

Summing up the two equations and integrating in time, we obtain:

$$\begin{aligned} \|\tau_2 \sqrt{\rho} \dot{\mathbf{u}}\|^2 + \|\sqrt{\rho} \mathbf{u}\|^2 + \|\tau_2 \mathbf{u}\|_{\mathbf{V}}^2 + \|\mathbf{W}\|_{\mathbf{V}}^2 + \|\sqrt{\tau_2 \tau_1 d_0} \varphi\|^2 + \|\sqrt{\tau_2 \mathbf{D}} \nabla \Psi\|^2 + \|\sqrt{d_0} \Psi\|^2 \\ + 2 \int_0^t \|\mathbf{u}\|_{\mathbf{V}_\delta}^2 + 2 \int_0^t \|\tau_2 \dot{\mathbf{u}}\|_{\mathbf{V}_\delta}^2 + 2 \int_0^t \|\sqrt{\tau_2 d_0} \varphi\|^2 + 2 \int_0^t \|\sqrt{\mathbf{D}} \nabla \Psi\|^2 + 2(\gamma \tau_2 \nabla \cdot \mathbf{u}, \Psi) \\ + 2 \int_0^t (d_0 \tau_1 \dot{\varphi}, \Psi) = I_0 + 2 \int_0^t (\tau_2^2 \mathbf{f}, \dot{\mathbf{u}}) + 2 \int_0^t (\tau_2 G, \varphi) + 2 \int_0^t (\mathbf{F}, \mathbf{u}) + 2 \int_0^t (G, \Psi), \end{aligned}$$

where $I_0 = \|\tau_2 \sqrt{\rho} \dot{\mathbf{u}}_0\|^2 + \|\sqrt{\rho} \mathbf{u}_0\|^2 + \|\tau_2 \mathbf{u}_0\|_{\mathbf{V}}^2 + \|\sqrt{\tau_2 \tau_1 d_0} \varphi_0\|^2$. First, we treat the forcing terms using integration by parts in time and Poincaré and Korn inequalities [37]:

$$\begin{aligned} 2 \int_0^t (\tau_2^2 \mathbf{f}, \dot{\mathbf{u}}) &\lesssim \int_0^t \left\| \frac{\tau_2 \mathbf{f}}{\sqrt{\mu \delta_1}} \right\|_*^2 + \int_0^t \|\tau_2 \dot{\mathbf{u}}\|_{\mathbf{V}_\delta}^2 \\ 2 \int_0^t (\tau_2 G, \varphi) &= -2 \int_0^t (\tau_2 g, \Psi) + 2(\tau_2 G, \Psi) \\ &\lesssim \int_0^t \frac{\|\tau_2 g\|_*^2}{\|\sqrt{\mathbf{D}}\|^2} + \int_0^t \|\sqrt{\mathbf{D}} \nabla \Psi\|^2 + \frac{\|\sqrt{\tau_2} G\|_*^2}{\|\sqrt{\mathbf{D}}\|^2} + \|\sqrt{\tau_2 \mathbf{D}} \nabla \Psi\|^2 \\ 2 \int_0^t (\mathbf{F}, \mathbf{u}) &\lesssim \int_0^t \left\| \frac{\mathbf{F}}{\sqrt{\mu \delta_1}} \right\|_*^2 + \int_0^t \|\mathbf{u}\|_{\mathbf{V}_\delta}^2 \\ 2 \int_0^t (G, \Psi) &\lesssim \int_0^t \frac{\|G\|_*^2}{\|\sqrt{\mathbf{D}}\|^2} + \int_0^t \|\sqrt{\mathbf{D}} \nabla \Psi\|^2. \end{aligned}$$

Then, we obtain:

$$\begin{aligned} \|\tau_2 \sqrt{\rho} \dot{\mathbf{u}}\|^2 + \|\sqrt{\rho} \mathbf{u}\|^2 + \|\tau_2 \mathbf{u}\|_{\mathbf{V}}^2 + \|\mathbf{W}\|_{\mathbf{V}}^2 + \|\sqrt{\tau_2 \tau_1 d_0} \varphi\|^2 + \|\sqrt{d_0} \Psi\|^2 + \int_0^t \|\mathbf{u}\|_{\mathbf{V}_\delta}^2 \\ + \int_0^t \|\tau_2 \dot{\mathbf{u}}\|_{\mathbf{V}_\delta}^2 + 2 \int_0^t \|\sqrt{\tau_2 d_0} \varphi\|^2 + 2(\gamma \tau_2 \nabla \cdot \mathbf{u}, \Psi) + 2 \int_0^t (d_0 \tau_1 \dot{\varphi}, \Psi) \lesssim I_0 \\ + \frac{\|\sqrt{\tau_2} G\|_*^2}{\|\sqrt{\mathbf{D}}\|^2} + \int_0^t \left\| \frac{\tau_2 \mathbf{f}}{\sqrt{\mu \delta_1}} \right\|_*^2 + \int_0^t \frac{\|\tau_2 g\|_*^2}{\|\sqrt{\mathbf{D}}\|^2} + \int_0^t \left\| \frac{\mathbf{F}}{\sqrt{\mu \delta_1}} \right\|_*^2 + \int_0^t \frac{\|G\|_*^2}{\|\sqrt{\mathbf{D}}\|^2}. \end{aligned} \quad (5)$$

We are left to control the tenth and eleventh terms on left hand side of (5). Concerning the first of the two, under assumption $\tau_2 \geq \tau_1$:

$$2 \int_0^t (d_0 \tau_1 \dot{\varphi}, \Psi) = \frac{d}{dt} \|\sqrt{\tau_1 d_0} \Psi\|^2 - 2 \int_0^t \|\sqrt{\tau_1 d_0} \varphi\|^2$$

For the second one, we test problem (4) by $(\tau_2 \mathbf{u}, 0)$ and we obtain:

$$\frac{1}{2} \frac{d}{dt} (\|\sqrt{\tau_2 \rho} \mathbf{u}\|^2 + \|\tau_2 \mathbf{W}\|_{\mathbf{V}}^2) + \|\tau_2 \mathbf{u}\|_{\mathbf{V}_\delta}^2 = (\gamma \tau_2 \nabla \cdot \mathbf{u}, \Psi) + (\tau_2 \mathbf{F}, \mathbf{u})$$

Finally, by substituting the two quantities into (5), we obtain that:

$$\begin{aligned} & \frac{d}{dt} (\|\sqrt{\tau_2 \rho} \mathbf{u}\|^2 + \|\tau_2 \mathbf{W}\|_{\mathbf{V}}^2 + \|\sqrt{\tau_1 d_0} \Psi\|^2) + \|\tau_2 \sqrt{\rho} \dot{\mathbf{u}}\|^2 + \|\sqrt{\rho} \mathbf{u}\|^2 + \left\| \frac{\tau_2}{2} \mathbf{u} \right\|_{\mathbf{V}}^2 + \|\tau_2 \mathbf{u}\|_{\mathbf{V}_\delta}^2 \\ & + \|\mathbf{W}\|_{\mathbf{V}}^2 + \|\sqrt{\tau_2 \tau_1 d_0} \varphi\|^2 + \|\sqrt{d_0} \Psi\|^2 + \int_0^t \|\mathbf{u}\|_{\mathbf{V}_\delta}^2 + \int_0^t \|\tau_2 \dot{\mathbf{u}}\|_{\mathbf{V}_\delta}^2 + 2 \int_0^t \|\sqrt{(\tau_2 - \tau_1) d_0} \varphi\|^2 \\ & \lesssim \|\mathbf{F}\|_*^2 + \frac{\|\sqrt{\tau_2} G\|_*^2}{\|\sqrt{\mathbf{D}}\|^2} + \int_0^t \left\| \frac{\tau_2 \mathbf{f}}{\sqrt{\mu \delta_1}} \right\|_*^2 + \int_0^t \frac{\|\tau_2 g\|_*^2}{\|\sqrt{\mathbf{D}}\|^2} + \int_0^t \left\| \frac{\mathbf{F}}{\sqrt{\mu \delta_1}} \right\|_*^2 + \int_0^t \frac{\|G\|_*^2}{\|\sqrt{\mathbf{D}}\|^2}. \end{aligned}$$

After a final integration in time and neglecting the positive integrals on the introduced auxiliary variables, we obtain the thesis. \square

Remark 1. *Theorem 3.1 provides two stability controls in $L^\infty((0, T_f], \mathbf{L}^2(\Omega))$ and $L^2((0, T_f], \mathbf{H}^1(\Omega))$ on the displacement solution \mathbf{u} . Concerning φ , we proved a control in $L^2((0, T_f], L^2(\Omega))$. Moreover, a final control for $\dot{\mathbf{u}}$ is provided in $L^2((0, T_f], \mathbf{L}^2(\Omega))$.*

Remark 2. *Theorem 3.1 provides a robust estimate with respect to the quasi-static case ($\rho = 0$). Moreover, the elastic case $\delta_1 = \delta_2 = 0$ is simple to be obtained by changing the control on the forcing term using Grönwall lemma [52].*

4 Polytopal discontinuous Galerkin discretization

This section aims to derive the fully-discrete scheme of problem (1). After introducing some preliminary concepts and assumptions about PolyDG methods, we detail the spatial discretization obtained via the PolyDG approximation, cf. Section 4.2. Then, for the time-integration of this problem, we consider two different cases, depending on the value of the time-relaxation parameter τ_1 . When $\tau_1 > 0$, both the equations in (1) are second-order hyperbolic, then we integrate in time with a Newmark- β scheme. When $\tau_1 = 0$, equation (1a) is second-order hyperbolic, while equation (1b) is parabolic, then we couple an implicit Newmark- β scheme for (1a), with a θ -method for (1b), cf. Section 4.3.

4.1 Preliminaries

First, we present the mesh assumptions, the discrete spaces, and some instrumental results for designing and analyzing PolyDG schemes. We introduce a subdivision \mathcal{T}_h of the computational domain Ω , whose elements are polygons/polyhedrons in dimension $d = 2, 3$, respectively. Next, we define the interfaces (or internal faces) as subsets of the intersection of any two neighboring elements of \mathcal{T}_h . If $d = 2$, an interface is a line segment, while if $d = 3$, an interface is a planar polygon that we assume can be further decomposed into a set of triangles. The same holds for the boundary faces collected in the set \mathcal{F}_B , which yields a simplicial subdivision of $\partial\Omega$. Accordingly, we define \mathcal{F}_I to be the set of internal faces and the set of all the faces as $\mathcal{F}_h = \mathcal{F}_B \cup \mathcal{F}_I$.

As a basis for constructing the PolyDG approximation, we define fully-discontinuous polynomial spaces on the mesh \mathcal{T}_h . Given an element-wise constant polynomial degree $\ell : \mathcal{T}_h \rightarrow \mathbb{N}_{>0}$, which determines the order of the approximation, the discrete spaces are defined such as

$$V_h^\ell = \left\{ v_h \in L^2(\Omega) : v_h|_\kappa \in \mathbb{P}^{\ell_\kappa}(\kappa) \quad \forall \kappa \in \mathcal{T}_h \right\}, \quad \mathbf{V}_h^\ell = \left[V_h^\ell \right]^d.$$

where, for each $\kappa \in \mathcal{T}_h$, the space $\mathbb{P}^{\ell_\kappa}(\kappa)$ is spanned by polynomials of maximum degree $\ell_\kappa = \ell_{|\kappa}$. To analyze the convergence of the spatial discretization, we consider a mesh sequence $\{\mathcal{T}_h\}_{h \rightarrow 0}$ satisfying the following properties:

Assumption 4.1. The mesh sequence $\{\mathcal{T}_h\}_h$ satisfies the following properties [36]:

A.1 Shape Regularity: $\forall K \in \mathcal{T}_h$ it holds : $c_1 h_K^d \lesssim |K| \lesssim c_2 h_K^d$.

A.2 Contact Regularity: $\forall F \in \mathcal{F}$ with $F \subseteq \overline{K}$ for some $K \in \mathcal{T}_h$, it holds $h_K^{d-1} \lesssim |F|$, where $|F|$ is the Hausdorff measure of the face F .

A.3 Submesh Condition: There exists a shape-regular, conforming, matching simplicial submesh $\widetilde{\mathcal{T}}_h$ such that:

- (i) $\forall \widetilde{K} \in \widetilde{\mathcal{T}}_h \quad \exists K \in \mathcal{T}_h$ such that $\widetilde{K} \subseteq K$.
- (ii) The family $\{\widetilde{\mathcal{T}}_h\}_h$ is shape and contact regular.
- (iii) $\forall \widetilde{K} \in \widetilde{\mathcal{T}}_h, K \in \mathcal{T}_h$ with $\widetilde{K} \subseteq K$, it holds $h_K \lesssim h_{\widetilde{K}}$.

We remark that under **A.1** the following inequality (called *discrete trace-inverse inequality*) holds (cf. [36] for all the details):

$$\|v\|_{L^2(\partial\kappa)} \lesssim \frac{\ell_\kappa}{h_\kappa^{1/2}} \|v\|_{L^2(\kappa)} \quad \forall v \in \mathbb{P}^{\ell_\kappa}(\kappa),$$

where the hidden constant is independent of ℓ_κ, h_κ , and the number of faces per element. In the following discussion, we introduce the Weighted Symmetric Interior Penalty method (WSIP) [38]. The key ingredient of this method is to exploit weighted averages instead of the arithmetic ones used in the standard Interior Penalty formulation, cf. [6, 64]. The use of weighted averages has been first introduced for elliptic problems in [61] and then developed for dG methods for dealing with advection-diffusion problems with locally vanishing diffusion [38]. In [19], the PolyDG-WSIP discretization of a thermo-hydronechanics problem is presented.

For the definition of the PolyDG-WSIP method, we introduce the weight function $\omega^+ : \mathcal{F}_I \rightarrow [0, 1]$ [43]. Given an interior face $F \in \mathcal{F}_I$, we denote the values taken by ω^+ and $\omega^- = 1 - \omega^+$ on the face F as $\omega|_F^+$ and $\omega|_F^-$, respectively. Given the function ω , we can introduce the notion of weighted averages and jump operators, denoted with $\{\{\cdot\}\}_\omega$ and $[[\cdot]]$, and normal jump, denoted with $[[\cdot]]_n$ [7, 38]:

$$\begin{aligned} [[a]] &= a^+ \mathbf{n}^+ + a^- \mathbf{n}^-, & [[\mathbf{a}]] &= \mathbf{a}^+ \odot \mathbf{n}^+ + \mathbf{a}^- \odot \mathbf{n}^-, & [[\mathbf{a}]]_n &= \mathbf{a}^+ \cdot \mathbf{n}^+ + \mathbf{a}^- \cdot \mathbf{n}^-, \\ \{\{a\}\}_\omega &= \omega^+ a^+ + \omega^- a^-, & \{\{\mathbf{a}\}\}_\omega &= \omega^+ \mathbf{a}^+ + \omega^- \mathbf{a}^-, & \{\{\mathbf{A}\}\}_\omega &= \omega^+ \mathbf{A}^+ + \omega^- \mathbf{A}^-, \end{aligned}$$

where $\mathbf{a} \odot \mathbf{n} = \mathbf{a} \mathbf{n}^T$ and $a, \mathbf{a}, \mathbf{A}$ are (regular enough) scalar-, vector-, and tensor-valued functions, respectively. The notation $(\cdot)^\pm$ is used for the trace on F taken within the interior of κ^\pm and \mathbf{n}^\pm is the outer unit normal vector to $\partial\kappa^\pm$. When the subscript ω is omitted, we consider $\omega^+ = \omega^- = 1/2$. Accordingly, on boundary faces $F \in \mathcal{F}_B$, we set

$$[[a]] = a\mathbf{n}, \quad \{\{a\}\}_\omega = a, \quad [[\mathbf{a}]] = \mathbf{a} \odot \mathbf{n}, \quad \{\{\mathbf{a}\}\}_\omega = \mathbf{a}, \quad [[\mathbf{a}]]_n = \mathbf{a} \cdot \mathbf{n}, \quad \{\{\mathbf{A}\}\}_\omega = \mathbf{A},$$

for the averages, this corresponds to consider ω^\pm single-valued and equal to 1.

From now on, for the sake of simplicity, we assume that the model parameters are element-wise constant. Moreover, for later use, we can introduce the quantities

$$\mu_\kappa = \mu|_\kappa, \quad \lambda_\kappa = \lambda|_\kappa, \quad \text{and} \quad \overline{\mathbf{D}}_\kappa = |\sqrt{\mathbf{D}}|_\kappa|_2^2,$$

where $|\cdot|_2$ denotes the ℓ^2 -norm in $\mathbb{R}^{d \times d}$.

4.2 Discontinuous Galerkin semi-discrete problem

The aim of this section is to introduce the PolyDG-WSIP approximation of problem (1) and to derive the stability estimate of the semi-discrete formulation. The PolyDG-WSIP semi-discretization of problem (2) reads: *for any $t \in (0, T_f]$, find $(\mathbf{u}_h, \varphi_h)(t) \in \mathbf{V}_h^\ell \times V_h^\ell$ such that $\forall (\mathbf{v}_h, \psi_h) \in \mathbf{V}_h^\ell \times V_h^\ell$:*

$$\begin{aligned} \mathcal{M}_u(\ddot{\mathbf{u}}_h, \mathbf{v}_h) + \mathcal{M}_{\varphi, \tau_1}(\ddot{\varphi}_h, \psi_h) + \mathcal{C}_{\tau_2, h}(\ddot{\mathbf{u}}_h, \psi_h) + \mathcal{A}_{e, \delta_1, h}(\dot{\mathbf{u}}_h, \mathbf{v}_h) + \mathcal{A}_{\text{div}, \delta_2, h}(\dot{\mathbf{u}}_h, \mathbf{v}_h) \\ + \mathcal{M}_\varphi(\dot{\varphi}_h, \psi_h) + \mathcal{C}_h(\dot{\mathbf{u}}_h, \psi_h) + \mathcal{A}_{e, h}(\mathbf{u}_h, \mathbf{v}_h) + \mathcal{A}_{\text{div}, h}(\mathbf{u}_h, \mathbf{v}_h) \\ + \mathcal{A}_{\varphi, h}(\varphi_h, \psi_h) - \mathcal{C}_h(\mathbf{v}_h, \varphi_h) = (\mathbf{f}, \mathbf{v}_h) + (g, \psi_h) \end{aligned} \quad (6)$$

supplemented by initial conditions $(\mathbf{u}_{h,0}, \varphi_{h,0}, \dot{\mathbf{u}}_{h,0}, \dot{\varphi}_{h,0})$ that are fitting approximations of the initial conditions of problem (1). The bilinear forms labelled with the subscript $_h$ appearing in (6) read

$$\begin{aligned} \mathcal{A}_{e, h}(\mathbf{u}, \mathbf{v}) = & (2\mu \boldsymbol{\epsilon}_h(\mathbf{u}), \boldsymbol{\epsilon}_h(\mathbf{v})) + \sum_{F \in \mathcal{F}_h} \int_F \sigma [[\mathbf{u}]] : [[\mathbf{v}]] \\ & - \sum_{F \in \mathcal{F}_h} \int_F (\{ \{ 2\mu \boldsymbol{\epsilon}_h(\mathbf{u}) \} \}_{\omega_\mu} : [[\mathbf{v}]] + [[\mathbf{u}]] : \{ \{ 2\mu \boldsymbol{\epsilon}_h(\mathbf{v}) \} \}_{\omega_\mu}), \end{aligned}$$

$$\begin{aligned} \mathcal{A}_{e, \delta_1, h}(\mathbf{u}, \mathbf{v}) = & (2\mu \delta_1 \boldsymbol{\epsilon}_h(\mathbf{u}), \boldsymbol{\epsilon}_h(\mathbf{v})) + \sum_{F \in \mathcal{F}_h} \int_F \sigma_{\delta_1} [[\mathbf{u}]] : [[\mathbf{v}]] \\ & - \sum_{F \in \mathcal{F}_h} \int_F (\{ \{ 2\mu \delta_1 \boldsymbol{\epsilon}_h(\mathbf{u}) \} \}_{\omega_{\delta_1}} : [[\mathbf{v}]] + [[\mathbf{u}]] : \{ \{ 2\mu \delta_1 \boldsymbol{\epsilon}_h(\mathbf{v}) \} \}_{\omega_{\delta_1}}), \end{aligned}$$

$$\begin{aligned} \mathcal{A}_{\text{div}, h}(\mathbf{u}, \mathbf{v}) = & (\lambda \nabla_h \cdot \mathbf{u}, \nabla_h \cdot \mathbf{v}) + \sum_{F \in \mathcal{F}_h} \int_F (\xi [[\mathbf{u}]]_{\mathbf{n}} [[\mathbf{v}]]_{\mathbf{n}}) \\ & - \sum_{F \in \mathcal{F}_h} \int_F (\{ \{ \lambda \nabla_h \cdot \mathbf{u} \} \}_{\omega_\lambda} [[\mathbf{v}]]_{\mathbf{n}} + [[\mathbf{u}]]_{\mathbf{n}} \{ \{ \lambda \nabla_h \cdot \mathbf{v} \} \}_{\omega_\lambda}), \end{aligned}$$

$$\begin{aligned} \mathcal{A}_{\text{div}, \delta_2, h}(\mathbf{u}, \mathbf{v}) = & (\lambda \delta_2 \nabla_h \cdot \mathbf{u}, \nabla_h \cdot \mathbf{v}) + \sum_{F \in \mathcal{F}_h} \int_F \xi_{\delta_2} [[\mathbf{u}]]_{\mathbf{n}} [[\mathbf{v}]]_{\mathbf{n}} \\ & - \sum_{F \in \mathcal{F}_h} \int_F (\{ \{ \lambda \delta_2 \nabla_h \cdot \mathbf{u} \} \}_{\omega_{\delta_2}} [[\mathbf{v}]]_{\mathbf{n}} + [[\mathbf{u}]]_{\mathbf{n}} \{ \{ \lambda \delta_2 \nabla_h \cdot \mathbf{v} \} \}_{\omega_{\delta_2}}), \end{aligned}$$

$$\begin{aligned} \mathcal{A}_{\varphi, h}(\varphi, \psi) = & (\mathbf{D} \nabla_h \varphi, \nabla_h \psi) + \sum_{F \in \mathcal{F}_h} \int_F \zeta [[\varphi]] \cdot [[\psi]] \\ & - \sum_{F \in \mathcal{F}_h} \int_F (\{ \{ \mathbf{D} \nabla_h \varphi \} \}_{\omega_{\mathbf{D}}} \cdot [[\psi]] + [[\varphi]] \cdot \{ \{ \mathbf{D} \nabla_h \psi \} \}_{\omega_{\mathbf{D}}} - \zeta [[\varphi]] \cdot [[\psi]]), \end{aligned}$$

$$\mathcal{C}_h(\mathbf{u}, \psi) = (\gamma \nabla_h \cdot \mathbf{u}, \psi) - \sum_{F \in \mathcal{F}_h} \int_F \{ \{ \psi \} \} [[\gamma \mathbf{u}]]_{\mathbf{n}},$$

$$\mathcal{C}_{\tau_2, h}(\mathbf{u}, \psi) = (\gamma \tau_2 \nabla_h \cdot \mathbf{u}, \psi) - \sum_{F \in \mathcal{F}_h} \int_F \{ \{ \psi \} \} [[\gamma \tau_2 \mathbf{u}]]_{\mathbf{n}}.$$

Here, for all $a \in V_h^\ell$ and $\mathbf{a} \in \mathbf{V}_h^\ell$, $\nabla_h a$ and $\nabla_h \cdot \mathbf{a}$ denote the broken differential operators whose restrictions to each element $\kappa \in \mathcal{T}_h$ are defined as $\nabla a|_\kappa$ and $\nabla \cdot \mathbf{a}|_\kappa$, respectively. Then, the broken version of the strain tensor is defined as $\boldsymbol{\epsilon}_h(\mathbf{u}) = (\nabla_h \mathbf{u} + \nabla_h \mathbf{u}^T) / 2$. We set:

$$\begin{aligned} \omega_\mu^\pm &= \frac{\mu^\mp}{\mu^+ + \mu^-}, & \omega_{\delta_1}^\pm &= \frac{(\mu\delta_1)^\mp}{(\mu\delta_1)^+ + (\mu\delta_1)^-}, & \omega_\lambda^\pm &= \frac{\lambda^\mp}{\lambda^+ + \lambda^-}, \\ \omega_{\delta_2}^\pm &= \frac{(\lambda\delta_2)^\mp}{(\lambda\delta_2)^+ + (\lambda\delta_2)^-}, & \omega_{\mathbf{D}}^\pm &= \frac{\eta_{\mathbf{D}_n}^\mp}{\eta_{\mathbf{D}_n}^+ + \eta_{\mathbf{D}_n}^-} \end{aligned}$$

where $\eta_{\mathbf{D}_n}^\pm = \mathbf{n}^{\pm T} \mathbf{D}^\pm \mathbf{n}^\pm$. The PolyDG-WSIP method requires the definition of the following stabilization functions $\sigma, \sigma_{\delta_1}, \xi, \xi_{\delta_2}, \zeta \in L^\infty(\mathcal{F}_h)$ are defined according to [38] as:

$$\begin{aligned} \sigma &= \begin{cases} \alpha_1 \gamma_\mu \max_{\kappa \in \{\kappa^+, \kappa^-\}} \left(\frac{\ell_\kappa^2}{h_\kappa} \right) & F \in \mathcal{F}_I, \\ \alpha_1 \mu_\kappa \ell_\kappa^2 h_\kappa^{-1} & F \in \mathcal{F}_B, \end{cases} & \sigma_{\delta_1} &= \begin{cases} \alpha_2 \gamma_{\delta_1} \max_{\kappa \in \{\kappa^+, \kappa^-\}} \left(\frac{\ell_\kappa^2}{h_\kappa} \right) & F \in \mathcal{F}_I, \\ \alpha_2 \mu_\kappa \delta_{1\kappa} \ell_\kappa^2 h_\kappa^{-1} & F \in \mathcal{F}_B, \end{cases} \\ \xi &= \begin{cases} \alpha_3 \gamma_\lambda \max_{\kappa \in \{\kappa^+, \kappa^-\}} \left(\frac{\ell_\kappa^2}{h_\kappa} \right) & F \in \mathcal{F}_I, \\ \alpha_3 \lambda_\kappa \ell_\kappa^2 h_\kappa^{-1} & F \in \mathcal{F}_B, \end{cases} & \xi_{\delta_2} &= \begin{cases} \alpha_4 \gamma_{\delta_2} \max_{\kappa \in \{\kappa^+, \kappa^-\}} \left(\frac{\ell_\kappa^2}{h_\kappa} \right) & F \in \mathcal{F}_I, \\ \alpha_4 \lambda_\kappa \delta_{2\kappa} \ell_\kappa^2 h_\kappa^{-1} & F \in \mathcal{F}_B, \end{cases} \\ \zeta &= \begin{cases} \alpha_5 \gamma_{\mathbf{D}} \max_{\kappa \in \{\kappa^+, \kappa^-\}} \left(\frac{\ell_\kappa^2}{h_\kappa} \right) & F \in \mathcal{F}_I, \\ \alpha_5 \overline{\mathbf{D}}_\kappa^{-1} \ell_\kappa^2 h_\kappa^{-1} & F \in \mathcal{F}_B, \end{cases} \end{aligned} \quad (7)$$

where $\alpha_1, \alpha_2, \alpha_3, \alpha_4, \alpha_5 \in \mathbb{R}$ are positive constants to be properly defined, ℓ_κ is the (local) polynomial degree of approximation, h_κ is the diameter of the element $\kappa \in \mathcal{T}_h$, and the coefficients $\gamma_\mu, \gamma_{\delta_1}, \gamma_\lambda, \gamma_{\delta_2}$, and $\gamma_{\mathbf{D}}$ are given by:

$$\begin{aligned} \gamma_\mu^\pm &= \frac{\mu^+ \mu^-}{\mu^+ + \mu^-}, & \gamma_{\delta_1}^\pm &= \frac{(\mu\delta_1)^+ (\mu\delta_1)^-}{(\mu\delta_1)^+ + (\mu\delta_1)^-}, \\ \gamma_\lambda^\pm &= \frac{\lambda^+ \lambda^-}{\lambda^+ + \lambda^-}, & \gamma_{\delta_2}^\pm &= \frac{(\lambda\delta_2)^+ (\lambda\delta_2)^-}{(\lambda\delta_2)^+ + (\lambda\delta_2)^-}, & \gamma_{\mathbf{D}} &= \frac{\eta_{\mathbf{D}_n}^+ \eta_{\mathbf{D}_n}^-}{\eta_{\mathbf{D}_n}^+ + \eta_{\mathbf{D}_n}^-}. \end{aligned}$$

Before writing the stability theorem in the semi-discrete version, we introduce the following auxiliary dG norms $\forall \mathbf{u} \in \mathbf{V}_h^\ell, \forall \varphi \in V_h^\ell$:

$$\begin{aligned} \|\mathbf{u}_h\|_{\text{dG},e}^2 &= \|\sqrt{2\mu}\boldsymbol{\epsilon}_h(\mathbf{u}_h)\|^2 + \|\sqrt{\lambda}\nabla_h \cdot \mathbf{u}_h\|^2 + \sum_{F \in \mathcal{F}} (\|\sqrt{\sigma} [[\mathbf{u}_h]]\|_F^2 + \|\sqrt{\xi} [[\mathbf{u}_h]]_{\mathbf{n}}\|_F^2), \\ \|\mathbf{u}\|_{\text{dG},\delta}^2 &= \|\sqrt{2\mu\delta_1}\boldsymbol{\epsilon}_h(\mathbf{u}_h)\|^2 + \|\sqrt{\lambda\delta_2}\nabla_h \cdot \mathbf{u}_h\|^2 + \sum_{F \in \mathcal{F}} (\|\sqrt{\sigma_{\delta_1}} [[\mathbf{u}_h]]\|_F^2 + \|\sqrt{\xi_{\delta_2}} [[\mathbf{u}_h]]_{\mathbf{n}}\|_F^2), \\ \|\varphi_h\|_{\text{dG},\varphi}^2 &= \|\sqrt{\mathbf{D}}\nabla_h \varphi_h\|^2 + \sum_{F \in \mathcal{F}} \|\sqrt{\zeta} [[\varphi_h]]\|_F^2. \end{aligned}$$

Theorem 4.1. Let us consider – for any time $t \in (0, T_f]$ – $(\mathbf{u}_h, \varphi_h)(t) \in \mathbf{V}_h^\ell \times V_h^\ell$ to be the solution of the semi-discrete problem (6) with homogeneous Dirichlet boundary conditions. Under Assumptions 3.1, 4.1, and assuming the following additional regularity on the forcing terms $\mathbf{f} \in C^0(0, T_f; \mathbf{L}^2(\Omega))$, $g \in C^0(0, T_f; L^2(\Omega))$, the following stability estimate holds:

$$\begin{aligned} \|\sqrt{\tau_2 \rho} \mathbf{u}_h\|^2 + \int_0^t \left(\|\tau_2 \sqrt{\rho} \dot{\mathbf{u}}_h\|^2 + \|\sqrt{\rho} \mathbf{u}_h\|^2 + \left\| \frac{\tau_2}{2} \mathbf{u}_h \right\|_{\text{dG},e}^2 + \|\tau_2 \mathbf{u}_h\|_{\text{dG},\delta}^2 + \|\sqrt{\tau_2 \tau_1 d_0} \varphi_h\|^2 \right) \lesssim \\ \|\sqrt{\tau_2 \rho} \mathbf{u}_{h,0}\|^2 + t I_{h,0} + \int_0^t \left(\|\mathbf{F}\|^2 + \frac{\|\sqrt{\tau_2} G\|^2}{\|\sqrt{\mathbf{D}}\|^2} + t \left\| \frac{\tau_2 \mathbf{f}}{\sqrt{\mu \delta_1}} \right\|^2 + t \frac{\|\tau_2 g\|^2}{\|\sqrt{\mathbf{D}}\|^2} + t \left\| \frac{\mathbf{F}}{\sqrt{\mu \delta_1}} \right\|^2 + t \frac{\|G\|^2}{\|\sqrt{\mathbf{D}}\|^2} \right), \end{aligned}$$

where $\mathbf{F} = \int_0^t \mathbf{f}$ and $G = \int_0^t g$, and $I_{h,0} = \|\tau_2 \sqrt{\rho} \dot{\mathbf{u}}_{h,0}\|^2 + \|\sqrt{\rho} \mathbf{u}_{h,0}\|^2 + \|\tau_2 \mathbf{u}_{h,0}\|_{\text{dG}}^2 + \|\sqrt{\tau_2 \tau_1 d_0} \varphi_{h,0}\|^2$. In this theorem, the (hidden) stability constant is independent of the physical parameters.

Proof. The proof of the stability can be adapted following the same steps of Theorem 3.1. The only differences are related to Poincarè and Korn's inequalities, for which we use their discrete version (cf. [21, 36]). \square

4.3 Time discretization

The aim of this section is to introduce the time discretization of the semi-discrete problem (6). The time-integration scheme depends on the parameters we consider in (1). Namely, when $\tau_1 > 0$, the system is second-order hyperbolic, and we choose to use a Newmark- β method for the whole system. When $\tau_1 = 0$, the second equation (1b) is parabolic, then we couple a Newmark- β method for the first equation with a θ -method for the second one. We denote by Newmark- β - θ the coupling of these two time-marching schemes.

By fixing a basis for the space $\mathbf{V}_h^\ell \times V_h^\ell$ and denoting by $[\mathbf{U}, \Phi]^T$ the vector of the expansion coefficients of the variables $(\mathbf{u}_h, \varphi_h)$, we can rewrite the semi-discrete problem (6) in the equivalent form:

$$\begin{bmatrix} \mathbf{M}_u & 0 \\ \mathbf{C}_{\tau_2} & \mathbf{M}_{\varphi, \tau_1} \end{bmatrix} \begin{bmatrix} \ddot{\mathbf{U}} \\ \ddot{\Phi} \end{bmatrix} + \begin{bmatrix} \mathbf{A}_{e, \delta_1} + \mathbf{A}_{\text{div}, \delta_2} & 0 \\ \mathbf{C} & \mathbf{M}_\varphi \end{bmatrix} \begin{bmatrix} \dot{\mathbf{U}} \\ \dot{\Phi} \end{bmatrix} + \begin{bmatrix} \mathbf{A}_e + \mathbf{A}_{\text{div}} & -\mathbf{C}^T \\ 0 & \mathbf{A}_\varphi \end{bmatrix} \begin{bmatrix} \mathbf{U} \\ \Phi \end{bmatrix} = \begin{bmatrix} \mathbf{F} \\ \mathbf{G} \end{bmatrix} \quad (8)$$

with initial conditions $\mathbf{U}(0) = \mathbf{U}_0$, $\dot{\mathbf{U}}(0) = \mathbf{U}_1$, $\Phi(0) = \Phi_0$, and (when $\tau_1 > 0$) $\dot{\Phi}(0) = \Phi_1$. The vectors \mathbf{F}, \mathbf{G} are representations of the linear functionals appearing on the right-hand side of (6).

To integrate (8) in time, we introduce a time-step $\Delta t = T_f/n$, with $n \in \mathbb{N}_{>0}$, discretize the interval $(0, T_f]$ as a sequence of time instants $\{t_k\}_{0 \leq k \leq n}$ such that $t_{k+1} - t_k = \Delta t$.

4.3.1 Case $\tau_1 > 0$ (Newmark- β method)

We start by defining $\mathbf{X}^k = \mathbf{X}(t^k)$, with $\mathbf{X} = [\mathbf{U}, \Phi]^T$. Next, we rewrite (8) in a compact form as $\mathbf{A}\ddot{\mathbf{X}} + \mathbf{B}\dot{\mathbf{X}} + \mathbf{C}\mathbf{X} = \mathbf{F}$ and derive

$$\ddot{\mathbf{X}} = \mathbf{A}^{-1} \left(\mathbf{F} - \mathbf{B}\dot{\mathbf{X}} - \mathbf{C}\mathbf{X} \right) = \mathbf{A}^{-1}\mathbf{F} - \mathbf{A}^{-1}\mathbf{B}\dot{\mathbf{X}} - \mathbf{A}^{-1}\mathbf{C}\mathbf{X} = \mathcal{L}(t, \mathbf{X}, \dot{\mathbf{X}}). \quad (9)$$

Last, we integrate in time (9) with the use of Newmark- β scheme, that exploits a Taylor expansion for \mathbf{X} and $\mathbf{Y} = \dot{\mathbf{X}}$:

$$\begin{cases} \mathbf{X}^{k+1} = \mathbf{X}^k + \Delta t \mathbf{Y}^k + \Delta t^2 \left(\beta_N \mathcal{L}^{k+1} + \left(\frac{1}{2} - \beta_N\right) \mathcal{L}^k \right), \\ \mathbf{Y}^{k+1} = \mathbf{Y}^k + \Delta t \left(\gamma_N \mathcal{L}^{k+1} + (1 - \gamma_N) \mathcal{L}^k \right), \end{cases}$$

where $\mathcal{L}^k = \mathcal{L}(t^k, \mathbf{X}^k, \dot{\mathbf{X}}^k)$ and the Newmark parameters β_N, γ_N satisfy: $0 \leq 2\beta_N \leq 1$, $0 \leq \gamma_N \leq 1$. The typical choices for the Newmark parameters, that ensure unconditionally stability and second-order accuracy for the scheme, are $\beta_N = 1/4$ and $\gamma_N = 1/2$. These are the values used in all the numerical tests of Section 5.

4.3.2 Case $\tau_1 = 0$ (Coupling Newmark- β and θ -methods)

In this second case, we adopt a coupling between a Newmark- β method for discretizing the first equation of (8) and a θ -method for the pressure equation. The complete calculations are reported in the appendix section A. For the sake of clarity, we report the final formulation in a compact form:

$$\mathbf{L}\mathbf{X}^{n+1} = \mathbf{R}\mathbf{X}^n + \mathbf{S}^{n+1} \quad n > 0, \quad (10)$$

where:

$$\mathbf{L} = \begin{bmatrix} \frac{1}{\beta_N \Delta t^2} \mathbf{M}_u + \mathbf{A}_u + \frac{\gamma_N}{\beta_N \Delta t} \mathbf{A}_{u,\delta} & -\mathbf{C}^T & 0 & 0 \\ \mathbf{C}_u & \frac{1}{\Delta t} \mathbf{M}_\varphi + \theta \mathbf{A}_\varphi & 0 & 0 \\ 0 & 0 & \mathbf{I} & -\Delta t \gamma_N \mathbf{I} \\ -\frac{1}{\beta_N \Delta t^2} \mathbf{I} & 0 & 0 & \mathbf{I} \end{bmatrix}$$

$$\mathbf{R} = \begin{bmatrix} \frac{1}{\beta_N \Delta t^2} \mathbf{M}_u + \frac{\gamma_N}{\beta_N \Delta t} \mathbf{A}_{u,\delta} & 0 & \frac{1}{\beta_N \Delta t} \mathbf{M}_u - \frac{\beta_N - \gamma_N}{\beta_N} \mathbf{A}_{u,\delta} & \frac{1-2\beta_N}{2\beta_N} \mathbf{M}_u - \frac{\Delta t(2\beta_N - \gamma_N)}{2\beta_N} \mathbf{A}_{u,\delta} \\ \mathbf{C}_u & \frac{1}{\Delta t} \mathbf{M}_\varphi - \tilde{\theta} \mathbf{A}_\varphi & \mathbf{C}_z & \mathbf{C}_a \\ 0 & 0 & \mathbf{I} & \Delta t(1 - \gamma_N) \mathbf{I} \\ -\frac{1}{\beta_N \Delta t^2} \mathbf{I} & 0 & -\frac{1}{\beta_N \Delta t} \mathbf{I} & \frac{2\beta_N - 1}{2\beta_N} \mathbf{I} \end{bmatrix}$$

$$\mathbf{X}^n = [\mathbf{U}^n, \mathbf{\Phi}^n, \mathbf{Z}^n, \mathbf{A}^n]^T \quad \mathbf{S}^{n+1} = [\mathbf{F}^{n+1}, \theta \mathbf{G}^{n+1} + \tilde{\theta} \mathbf{G}^n, 0, 0]^T$$

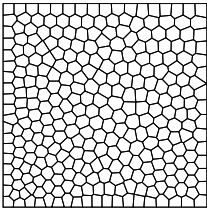
Remark 3. From an operative point of view, we do not solve the whole system (10). For the sake of reducing the overall computational cost, we solve it just for \mathbf{U}^{n+1} , $\mathbf{\Phi}^{n+1}$. Then, we update the values of \mathbf{A}^{n+1} and \mathbf{Z}^{n+1} .

5 Numerical results

This section aims to assess the performance of the proposed scheme in terms of accuracy and robustness with respect to the model parameters. Then, we test the method by addressing some benchmark and literature test cases. The numerical implementation is carried out in the open-source `lymph` library [5], implementing the PolyDG method for multiphysics. In all the tests, the PolyDG space discretization is solved monolithically, and it is coupled with the Newmark- β method when $\tau_1 > 0$ and with a coupled Newmark- β - θ -method when $\tau_1 = 0$ (cf. Section 4.3) for time integration. The parameters of the Newmark- β and θ -method are $\gamma_N = 1/2$, $\beta_N = 1/4$, and $\theta = 1/2$. All the penalty coefficients α_i , $i = 1, 2, \dots, 5$ in (7) are set equal to 10.

5.1 Convergence tests

Convergence vs space discretization parameters. The aim of this section is to assess the performance of the proposed scheme in terms of accuracy with respect to the space discretization parameters, i.e., the mesh size h and the polynomial degree of approximation ℓ . We consider problem (1) in the square



Coefficient	Value	Coefficient	Value
ρ [kg m ⁻³]	1	γ [-]	1
μ [Pa]	1	λ [Pa]	1
d_0 [Pa ⁻¹]	1	\mathbf{D} [m ² Pa ⁻¹ s ⁻¹]	\mathbf{I}
δ_1 [s]	1	δ_2 [s]	1
τ_1 [s]	1	τ_2 [s]	1

Figure 1: Convergence test: example of a 2D Voronoi polygonal mesh made of 300 elements.

Table 2: Convergence test: problem parameters for the convergence analysis

domain $\Omega = (0, 1)^2$ with manufactured analytical solutions:

$$\mathbf{u} = \sin(2\pi t) \begin{bmatrix} x^2 \sin(\pi x) \sin(\pi y) \\ -x^2 \sin(\pi x) \sin(\pi y) \end{bmatrix}, \quad \varphi = \sin(\sqrt{2}\pi t) \left(x^2 \cos\left(\frac{\pi x}{2}\right) \sin(\pi x) \right).$$

The initial and boundary conditions and the forcing terms are inferred from the exact solutions. The model coefficients are chosen as reported in Table 2. We remark that - for completeness - we also assess the method's performance for the case $\tau_1 = 0$.

For the h -convergence, a sequence of polygonal meshes in Figure 1 is considered, and we consider polynomial degree $\ell = 3$. At the same time, for the ℓ -convergence we fix a computational mesh of 100 elements and vary the polynomial degree $\ell = 1, 2, \dots, 5$. The time discretization parameters are $T_f = 0.1$, $\Delta t = 5 \cdot 10^{-5}$.

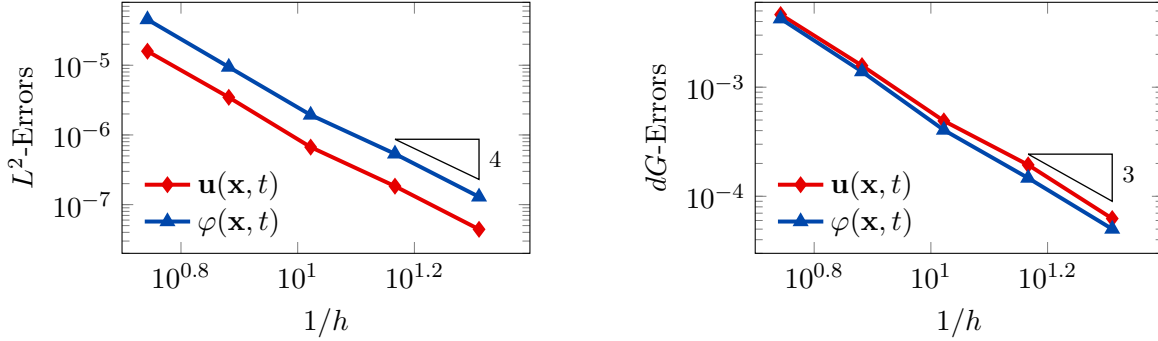


Figure 2: Convergence test vs h ($\tau_1 = 1$): computed errors in L^2 -norm (left) and dG -norm (right) versus $1/h$ (\log - \log scale). The errors are computed at the final time T_f . The polynomial degree of approximation is taken as $\ell = 3$.

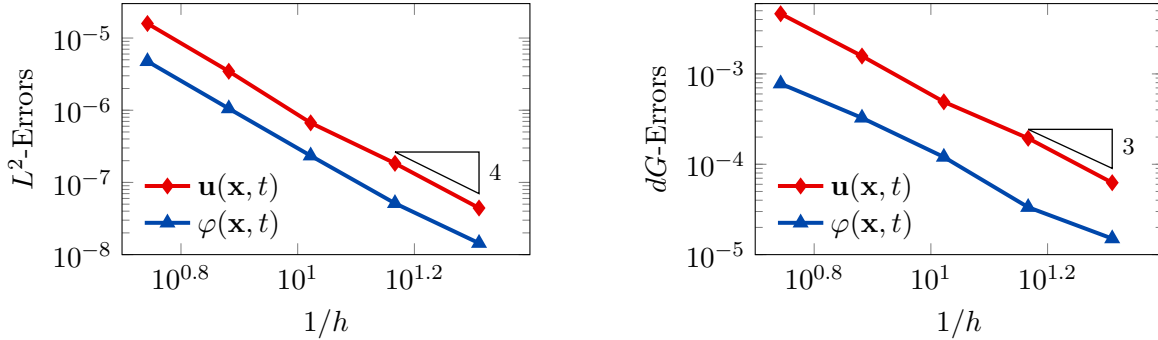


Figure 3: Convergence test vs h ($\tau_1 = 0$): computed errors in L^2 -norm (left) and dG -norm (right) versus $1/h$ (\log - \log scale). The errors are computed at the final time T_f . The polynomial degree of approximation is taken as $\ell = 3$.

In Figure 2, we report the L^2 and dG -errors for the two unknowns with respect to the mesh size (\log - \log scale). In agreement with the results expected by the theory of the PolyDG methods (cf. [25, 26]), we observe that, as we are using $\ell = 3$, the dG -errors show a convergence rate proportional to h^3 . Moreover, concerning the L^2 -errors, we observe that the errors decay as $h^{\ell+1}$. In Figure 3, we report the results for the same convergence test, but taking $\tau_1 = 0$ in (1b). Also, for this configuration, the numerical results match the predicted convergence rates of the PolyDG framework.

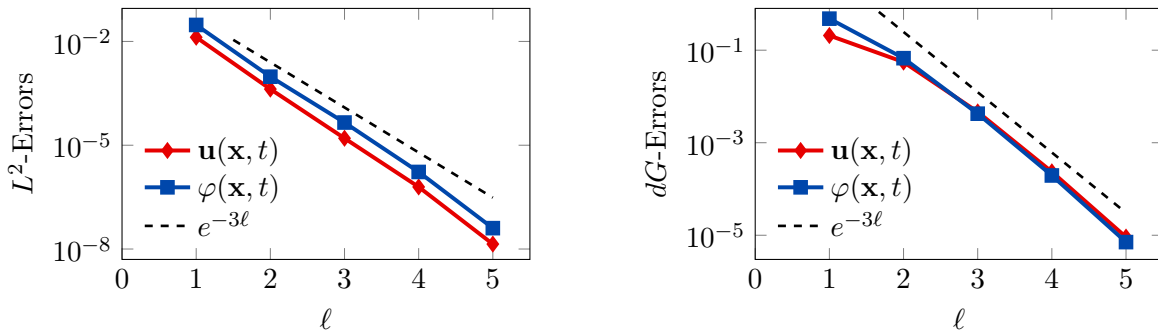


Figure 4: Convergence test vs ℓ ($\tau_1 = 1$): computed errors in L^2 -norm (left) and dG -norm (right) versus ℓ (semi-log scale). The errors are computed at the final time T_f . The computational mesh is made of 100 polygons.

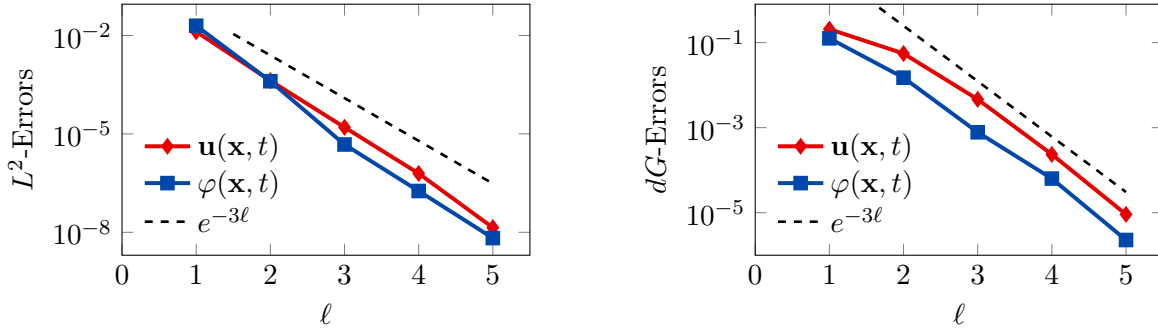


Figure 5: Convergence test vs ℓ ($\tau_1 = 0$): computed errors in L^2 -norm (left) and dG -norm (right) versus ℓ (*semi-log* scale). The errors are computed at the final time T_f . The computational mesh is made of 100 polygons.

In Figure 4, Figure 5, we report the results for the ℓ -convergence test. We observe that, for both the model configurations, the errors of the two variables decay exponentially.

Convergence vs time discretization parameter. This section aims to assess the performance of the proposed scheme in terms of accuracy with respect to the time-step Δt . To focus on the time-marching scheme, we consider problem (1) in the square domain $\Omega = (0, 1)^2$ with manufactured analytical solutions

$$\mathbf{u} = \sin(2\pi t) \begin{bmatrix} x + y \\ 3x - 5y \end{bmatrix}, \quad \varphi = \sin(\sqrt{2}\pi t) (10x + 6y).$$

The initial conditions, boundary conditions, and forcing terms are inferred from the exact solutions. The model coefficients are chosen as reported in Table 2. To test the convergence of the scheme with respect to Δt (both for the Newmark- β and for the coupled Newmark- β - θ method), we fix a mesh of $N = 100$ elements with $\ell = 1$, and we fix the final time $T_f = 0.1$. Then, we vary the time-step parameter.

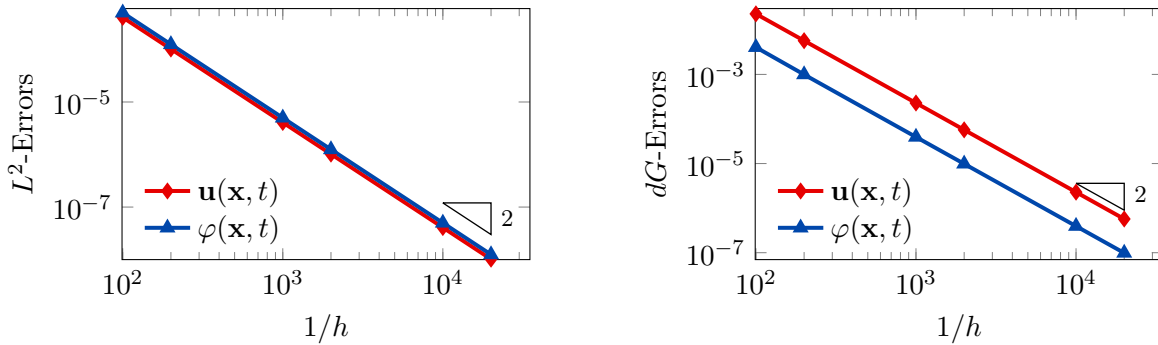


Figure 6: Convergence test vs Δt ($\tau_1 = 1$): computed errors in L^2 -norm (left) and dG -norm (right) versus $1/h$ (*log-log* scale). The errors are computed at the final time T_f . The time-marching scheme is the Newmark- β method.

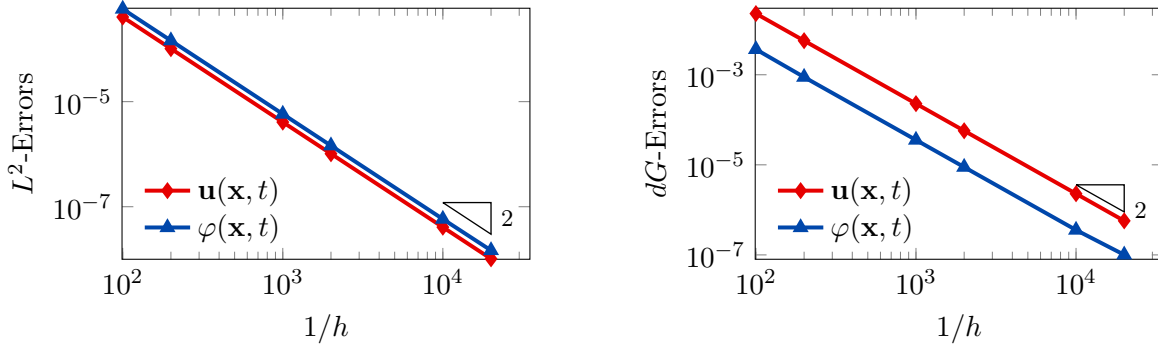


Figure 7: Convergence test vs Δt ($\tau_1 = 0$): computed errors in L^2 -norm (left) and dG -norm (right) versus $1/h$ (log-log scale). The errors are computed at the final time T_f . The time-marching scheme is the coupled Newmark- β and θ -method.

In Figure 6, Figure 7, we report the results for the convergence against the time-step Δt . We observe that for both the Newmark- β scheme ($\tau_1 \neq 0$) and for the coupled Newmark- β - θ time-marching schemes ($\tau_1 = 0$), we have second-order accuracy. The time-integration schemes' parameters we used in this test are $\gamma_N = 1/2$, $\beta_N = 1/4$, and $\theta = 1/2$, as these choices ensure unconditional stability and second-order accuracy.

5.2 Superconvergence tests

The aim of this section is to prove that the PolyDG scheme proposed for this problem is not only optimal convergence, but it also shows some superconvergence properties. To this aim, we consider the following exact solutions:

$$\begin{aligned} \mathbf{u}(x, y, t) &= \nu_u \sin(2\pi t) \begin{pmatrix} x^2 \sin(\pi x) \sin(\pi y) \\ -x^2 \sin(\pi x) \sin(\pi y) \end{pmatrix}, \\ \varphi(x, y, t) &= \nu_\varphi \sin(\sqrt{2}\pi t) \left(x^2 \cos\left(\frac{\pi x}{2}\right) \sin(\pi x) \right), \end{aligned}$$

from which we infer initial and boundary conditions, as well as forcing terms. The parameters ν_u , ν_φ control the magnitude of the displacement and the generalized pressure, respectively. The model coefficients are reported in Table 2 (chosen as in the convergence test). We observe that the optimal convergence property has been already proven in Section 5.1 by setting $\nu_u = \nu_\varphi = 1$.

To observe the better robustness of the scheme with respect to large pressures, we propose two different tests. In the first, we set $\nu_u = 0.1$, $\nu_\varphi = 10^4$, we consider the same sequence of meshes as in Section 5.1 and polynomial degree $\ell = 2$. For the second test, we fix $\nu_u = 0.1$, the mesh, and the polynomial degree of approximation; then we vary the values of $\nu_\varphi = [1, 10^1, 10^2, 10^3, 10^4, 10^5, 10^6]$. We consider the following discretization parameters for the second test: $N = 400$, $\ell = 2$.

$1/h$	$\ \mathbf{e}^u\ _{L^2}$	$\text{roc}_{L^2}^u$	$\ \mathbf{e}^u\ _{dG}$	roc_{dG}^u	$\ e^p\ _{L^2}$	$\text{roc}_{L^2}^p$	$\ e^p\ _{dG}$	roc_{dG}^p
5.53	$4.49 \cdot 10^{-3}$	-	0.15	-	8.47	-	1411.33	-
7.62	$1.06 \cdot 10^{-3}$	4.49	0.06	3.11	2.83	3.42	779.86	1.85
10.53	$2.86 \cdot 10^{-4}$	4.06	0.02	3.48	0.85	3.73	373.68	2.28
14.68	$9.30 \cdot 10^{-5}$	3.38	$7.47 \cdot 10^{-3}$	2.69	0.36	2.62	196.18	1.94
20.45	$3.12 \cdot 10^{-5}$	3.30	$2.70 \cdot 10^{-3}$	3.07	0.12	3.19	96.92	2.13

Table 3: Superconvergence test: computed errors and convergence rates in L^2 - and dG -norms versus h using as polynomial degree of approximation $\ell = 2$.

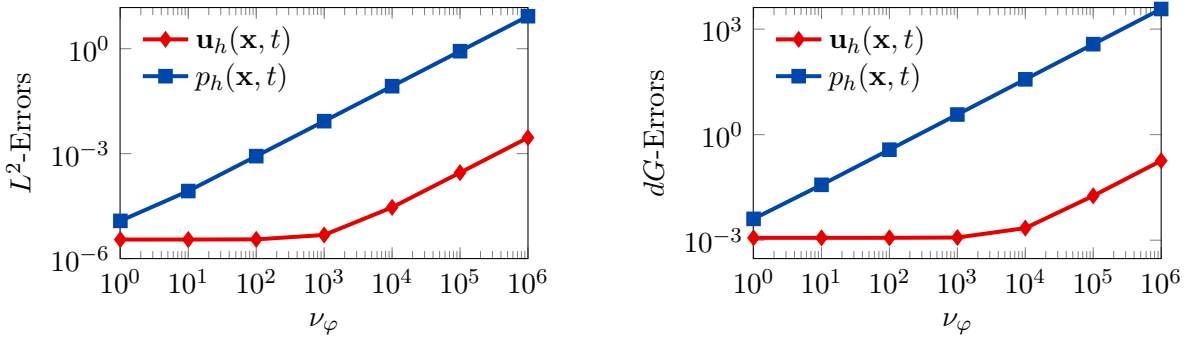


Figure 8: Superconvergence test: computed errors in L^2 -norm (left) and dG -norm (right) versus ν_φ (\log - \log scale) using as polynomial degrees of approximation and number of elements: $\ell = 2$, $N = 400$.

By looking at Table 3 we observe the superconvergence phenomenon for the displacement field. Indeed, we observe that using a polynomial degree of approximation equal to ℓ , then the error of the displacement in dG -norm converges with order $\ell + 1$ (we remark that the expected order is ℓ in this case [25, 26]; this rate is observed for the generalized-pressure). Moreover, for what concerns the error in L^2 -norm, we observe $(\ell + 1) + 1$ convergence rate for the first refinements.

In Figure 8, we observe the behavior of the errors with respect to increasing values of ν_φ . We see that both the L^2 - and dG -errors of the displacements are way lower than the errors of the generalized pressure (even for not too big values of ν_φ). It is interesting to notice that, for the first tested values of ν_φ , the displacement errors remain almost constant while the errors of the generalized pressure start growing.

5.3 Robustness tests

In this section, we address the problem of testing the scheme's robustness with respect to some of the physical parameters appearing in (1). In particular, we are interested in testing the robustness with respect to low values of the permeability \mathbf{D} and high values of secondary consolidation $\delta_2\lambda$ and for the latter, possibly considering low values of the storage coefficient d_0 . The values of the other model parameters are as in Table 2. The time discretization parameters are $T_f = 0.1$, $\Delta t = 5 \cdot 10^{-5}$. For the robustness analysis, a sequence of polygonal meshes as the one in Figure 1 is considered and we consider polynomial degree $\ell = 3$.

$1/h$	$\ \mathbf{e}^u\ _{L^2}$	$\text{roc}_{L^2}^u$	$\ \mathbf{e}^u\ _{dG}$	roc_{dG}^u	$\ e^p\ _{L^2}$	$\text{roc}_{L^2}^p$	$\ e^p\ _{dG}$	roc_{dG}^p
5.53	$1.58 \cdot 10^{-5}$	-	$4.63 \cdot 10^{-3}$	-	$5.98 \cdot 10^{-4}$	-	$1.77 \cdot 10^{-4}$	-
7.62	$3.46 \cdot 10^{-6}$	4.74	$1.58 \cdot 10^{-3}$	3.36	$1.89 \cdot 10^{-4}$	3.59	$7.22 \cdot 10^{-5}$	2.80
10.53	$6.67 \cdot 10^{-7}$	5.10	$4.91 \cdot 10^{-4}$	3.61	$5.19 \cdot 10^{-5}$	4.01	$2.95 \cdot 10^{-5}$	2.77
14.68	$1.84 \cdot 10^{-7}$	3.88	$1.94 \cdot 10^{-4}$	2.79	$2.00 \cdot 10^{-5}$	2.87	$1.45 \cdot 10^{-5}$	2.14
20.45	$4.42 \cdot 10^{-8}$	4.30	$6.25 \cdot 10^{-5}$	3.42	$6.58 \cdot 10^{-6}$	3.35	$6.90 \cdot 10^{-6}$	2.24

Table 4: Robustness test vs conductivity: polynomial degree $\ell = 3$. The parameters are chosen as in Table 2 and the conductivity is set as $\mathbf{D} = 10^{-6}\mathbf{I}$.

$1/h$	$\ \mathbf{e}^u\ _{L^2}$	$\text{roc}_{L^2}^u$	$\ \mathbf{e}^u\ _{dG}$	roc_{dG}^u	$\ e^p\ _{L^2}$	$\text{roc}_{L^2}^p$	$\ e^p\ _{dG}$	roc_{dG}^p
5.53	$3.74 \cdot 10^{-4}$	-	0.02	-	$2.00 \cdot 10^{-5}$	-	$2.72 \cdot 10^{-3}$	-
7.62	$1.31 \cdot 10^{-4}$	3.28	$8.99 \cdot 10^{-3}$	1.90	$5.63 \cdot 10^{-6}$	3.94	$1.03 \cdot 10^{-3}$	3.02
10.53	$3.36 \cdot 10^{-5}$	4.21	$3.20 \cdot 10^{-3}$	3.20	$1.28 \cdot 10^{-6}$	4.58	$3.28 \cdot 10^{-4}$	3.55
14.68	$6.66 \cdot 10^{-6}$	4.86	$9.37 \cdot 10^{-4}$	3.69	$3.69 \cdot 10^{-7}$	3.75	$1.18 \cdot 10^{-4}$	3.09
20.45	$2.11 \cdot 10^{-6}$	3.47	$3.98 \cdot 10^{-4}$	2.579	$8.46 \cdot 10^{-8}$	4.44	$4.04 \cdot 10^{-5}$	3.22

Table 5: Robustness test vs secondary consolidation: polynomial degree $\ell = 3$. The parameters are chosen as in Table 2 and the secondary consolidation coefficient is set as $\delta_2\lambda = 10^6$.

$1/h$	$\ \mathbf{e}^u\ _{L^2}$	$\text{roc}_{L^2}^u$	$\ \mathbf{e}^u\ _{dG}$	roc_{dG}^u	$\ e^p\ _{L^2}$	$\text{roc}_{L^2}^p$	$\ e^p\ _{dG}$	roc_{dG}^p
5.53	$3.74 \cdot 10^{-4}$	-	0.02	-	0.01	-	1.06	-
7.62	$1.31 \cdot 10^{-4}$	3.28	$8.99 \cdot 10^{-3}$	1.90	$3.00 \cdot 10^{-3}$	4.65	0.33	3.59
10.53	$3.36 \cdot 10^{-5}$	4.21	$3.20 \cdot 10^{-3}$	3.20	$4.62 \cdot 10^{-4}$	5.92	0.07	4.71
14.68	$6.68 \cdot 10^{-6}$	4.85	$9.36 \cdot 10^{-4}$	3.69	$1.07 \cdot 10^{-4}$	4.41	0.02	3.59
20.45	$2.20 \cdot 10^{-6}$	3.35	$3.98 \cdot 10^{-4}$	2.58	$6.10 \cdot 10^{-5}$	1.68	$5.00 \cdot 10^{-3}$	4.45

Table 6: Robustness test vs secondary consolidation: polynomial degree $\ell = 3$. The parameters are chosen as in Table 2, the secondary consolidation coefficient is set as $\delta_2\lambda = 10^6$, and the storage coefficient is set as $d_0 = 10^{-6}$.

First, comparing the results for low values of conductivity \mathbf{D} (cf. Table 4) with classical error estimates of the PolyDG methods (see also Section 5.1), we observe that our scheme is robust with respect to this configuration. We observe that we lose $\ell + 1$ accuracy in L^2 -norm for the generalized pressure, but we still observe convergence of order ℓ . For what concerns the dG -error analysis, we observe a decrease of the dG -errors of the pressure when refining the mesh. However, we observe that their values are affected by the fact that the conductivity value enters the norm's definition. Then, we observe the performance of the method for high values of the secondary consolidation coefficient $\delta_2\lambda$, considering both the cases in which we have not-degenerating and degenerating storage coefficient d_0 . The method is robust in both regimes; however – as expected – it behaves slightly worse when the storage coefficient is $\ll 1$.

5.4 Wave propagation in thermo-elastic media

This section considers a wave propagation problem in thermoelastic media inspired by [28]. The aim of this simulation is to prove that the proposed scheme can reproduce known results present in the literature for the thermoelastic framework and can give *physically-sound* results.

Vertical source term. We consider a domain $\Omega = (0 \text{ m}, 2310 \text{ m})^2$ with the thermoelastic properties reported in Table 7 [28].

Coefficient	Value	Coefficient	Value
ρ [kg m ⁻³]	2650	β [Pa K ⁻¹]	79200
μ [Pa]	$6 \cdot 10^9$	λ [Pa]	$4 \cdot 10^9$
a_0 [Pa K ⁻²]	117	Θ [m ² Pa K ⁻² s ⁻¹]	10.5 I
τ_1 [s]	$1.49 \cdot 10^{-8}$	τ_2 [s]	$1.49 \cdot 10^{-8}$
δ_1 [s]	0	δ_2 [s]	0

Table 7: Wave propagation in thermoelastic media: homogeneous medium properties

In the first test case, we consider a vertical source term \mathbf{f} in (1a). The source is set in the computational domain's center and multiplied by a time-history function $h(t)$. In our case, the time evolution is given by [28] $h(t) = A_0 \cos[2\pi(t - t_0)f_0] \exp[-2(t - t_0)^2 f_0^2]$, where $A_0 = 10^4$ m is the amplitude, $f_0 = 5$ Hz is the peak-frequency, and $t_0 = 3/(2f_0) = 0.3$ s is the time-shift. We adopt a polygonal mesh with mesh size $h \sim 76$ m (3500 elements) and polynomial degree $\ell = 4$. As a time-stepping scheme we employ the Newmark- β scheme, with $\Delta t = 5 \cdot 10^{-4}$ s and $T_f = 0.5$ s. Finally, we complete our problem with homogeneous Dirichlet boundary conditions and null initial conditions. In the following, we denote by \mathbf{v}_h the solid velocity (i.e. $\dot{\mathbf{u}}_h$) and by $v_{h,y}$ its vertical component.

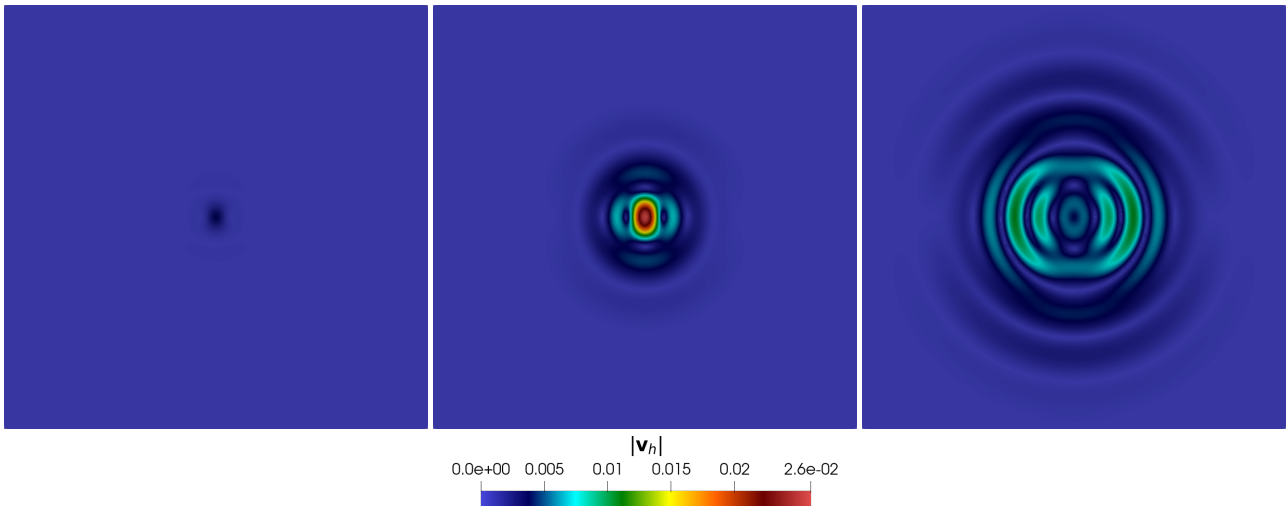


Figure 9: Wave propagation in thermoelastic media with vertical source term: computed velocity field $|\mathbf{v}_h|$ at the time instants $t = 0.1$ s (left), $t = 0.3$ s (center), $t = 0.5$ s (right).

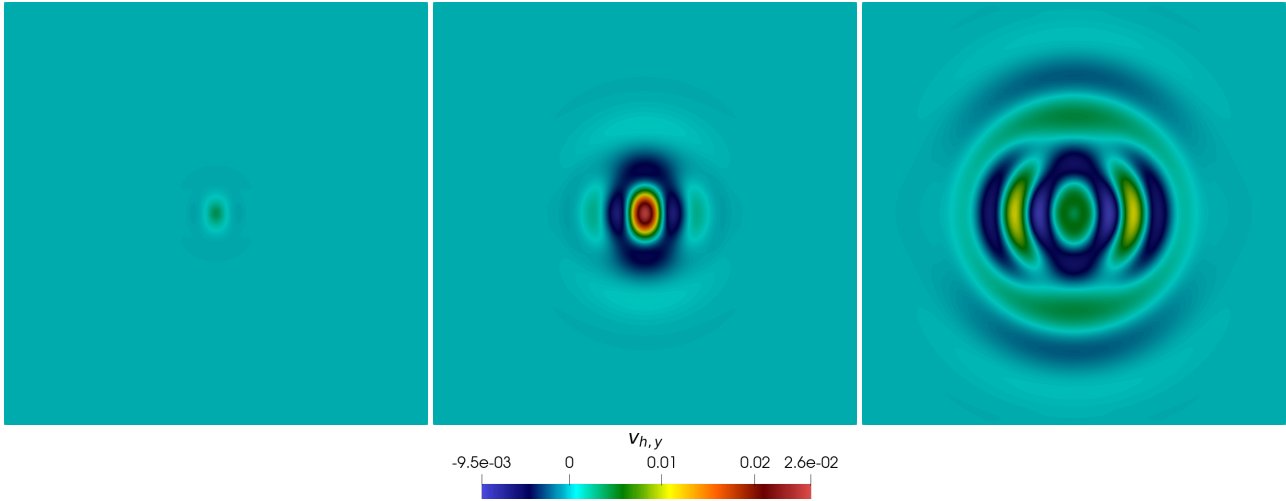


Figure 10: Wave propagation in thermoelastic media with vertical source term: computed vertical component of the velocity field $v_{h,y}$ at the time instants $t = 0.1$ s (left), $t = 0.3$ s (center), $t = 0.5$ s (right).

From the results of Figure 9 we observe a symmetric wavefront that detaches from the center of the domain symmetric to the x - and y -axes. This behavior is correct due to the form of the forcing term we are imposing. Looking at the three snapshots, we can observe the presence of the elastic E -wave captured by our scheme and the S -wave. The presence of these two waves is more evident by looking at Figure 10, where the computed vertical velocity field is reported. Indeed, it is possible to observe the propagation of the E wave, traveling faster and along the y -direction, and the propagation of the S -waves that are slower and propagate along the x -direction. Last, in Figure 11, we observe the propagation of the diffusive T -wave, that is originated by a vertical source term in the momentum conservation equation. A thermal source term in the energy conservation equation is not considered here. In conclusion, considering the different central peak frequencies f_0 , we can see a good agreement

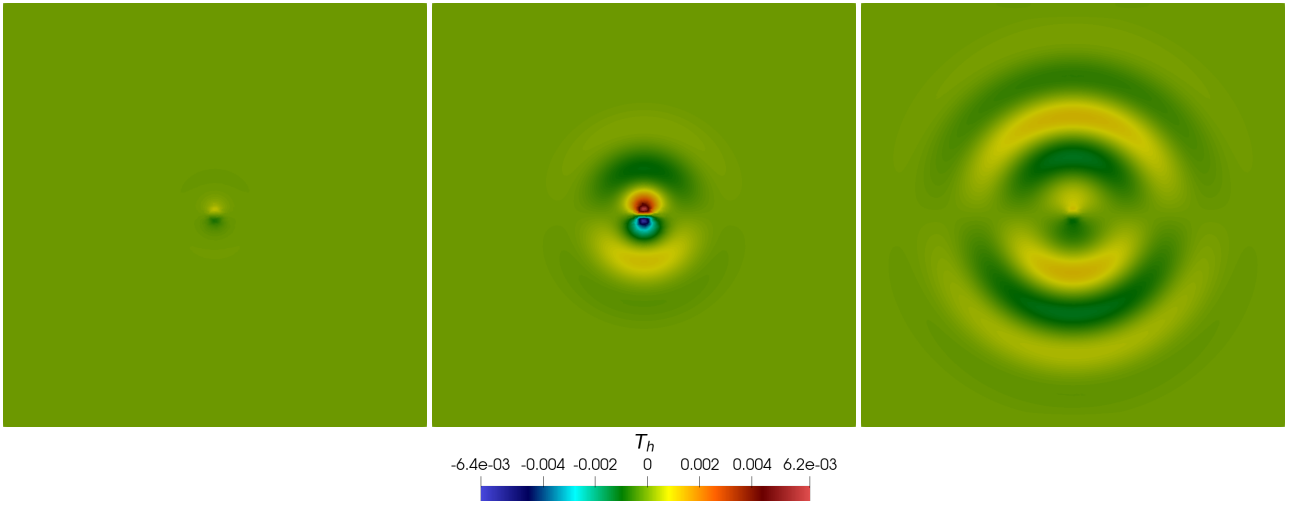


Figure 11: Wave propagation in thermoelastic media with vertical source term: computed temperature field T_h at the time instants $t = 0.1\text{s}$ (left), $t = 0.3\text{s}$ (center), $t = 0.5\text{s}$ (right).

between our results and those presented in [27].

Shear source term. In the second test case, we model the forcing term of the momentum equation \mathbf{f} as a shear source. The forcing term is modeled as $\mathbf{f} = -\mathbf{M} \nabla \cdot \delta(\mathbf{x} - \mathbf{x}_s) h(t)$ [47], where \mathbf{M} is a moment tensor, \mathbf{x}_s is the point-source location, $\delta(\mathbf{x} - \mathbf{x}_s)$ is the Kronecker delta located in \mathbf{x}_s , and $h(t)$ is the aforementioned time-history function. We consider \mathbf{M} a tensor with zero components on the diagonal and not zero components off-diagonal; this choice induces the presence of shear waves and generally has a strong connection with the wave patterns we observe. A momentum source of this shape is often used in the context of earthquakes. The properties of the medium and the discretization parameters are chosen as in the vertical source term test.

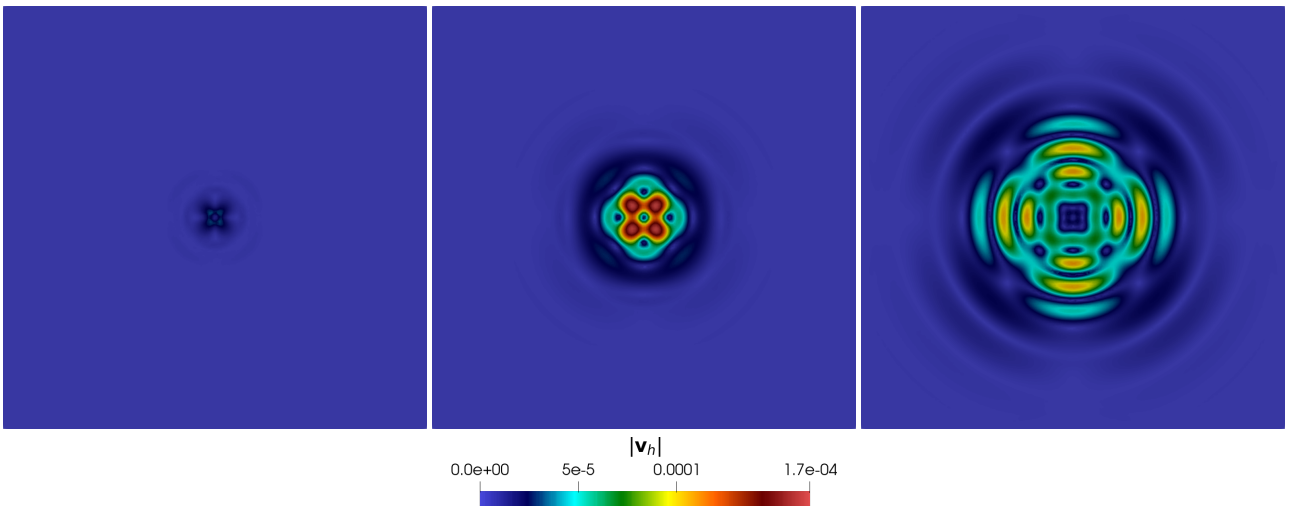


Figure 12: Wave propagation in thermoelastic media with shear source term: computed velocity field $|\mathbf{v}_h|$ at the time instants $t = 0.1\text{s}$ (left), $t = 0.3\text{s}$ (center), $t = 0.5\text{s}$ (right)

From the results of Figure 12 we notice a symmetric wavefront that detaches from the center of the domain. The velocity field has a symmetric pattern with respect to the diagonals of the domain (due to the choice of the forcing term). Looking at the three snapshots, we observe the propagation of the elastic wave. From the results in Figure 13, we notice the presence of shear waves and the anti-symmetric pattern of the wave fronts with respect to the y -axis. In Figure 14, we can see the presence of the diffusive thermal T -wave, which has a symmetric pattern with respect to the diagonals of the domain and antisymmetric with respect to the x - and y -axis. The results we obtain for this test are coherent with [28] (thermoelasticity) and [18, 27] (thermo-poroelasticity).

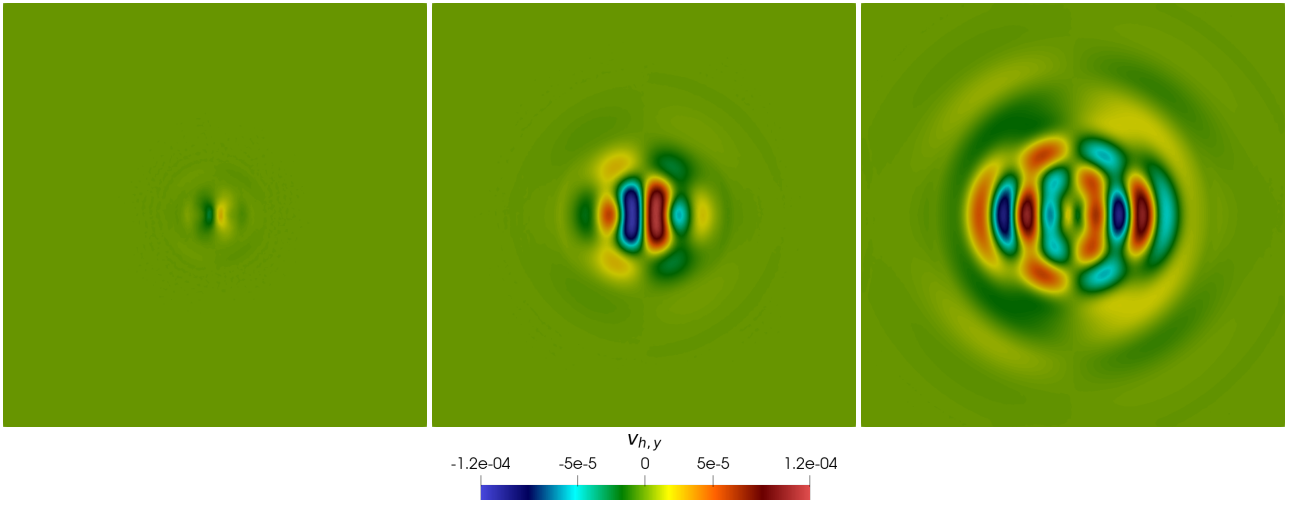


Figure 13: Wave propagation in thermoelastic media with shear source term: computed vertical component of the velocity field $v_{h,y}$ at the time instants $t = 0.1s$ (left), $t = 0.3s$ (center), $t = 0.5s$ (right).

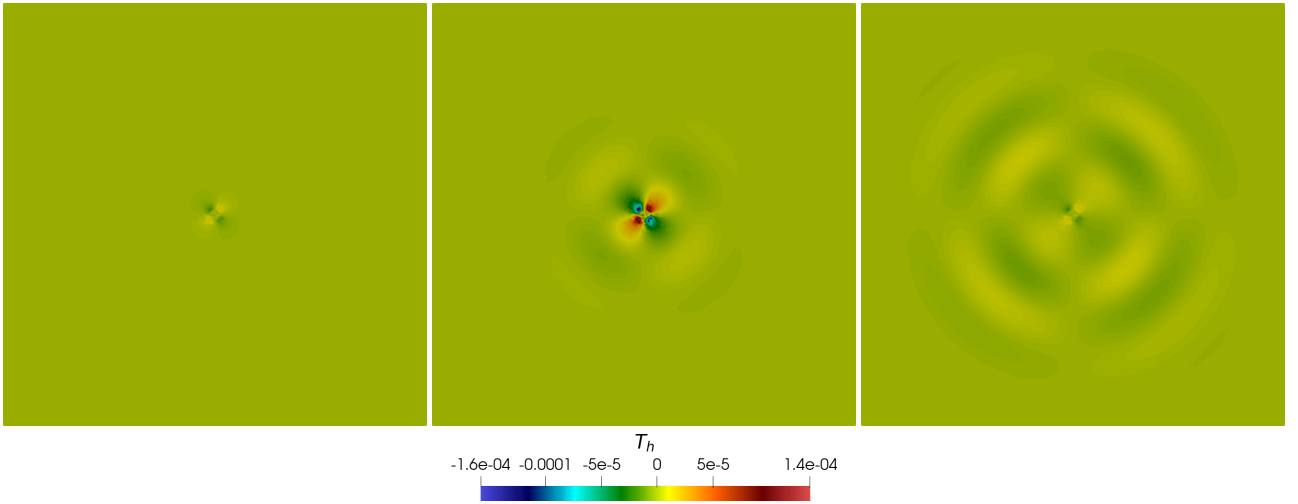


Figure 14: Wave propagation in thermoelastic media with shear source term: computed temperature field T_h at the time instants $t = 0.1s$ (left), $t = 0.3s$ (center), $t = 0.5s$ (right).

Shear source term in a heterogeneous media. In this last thermoelastic test case, we model the thermoelastic wave propagation in a heterogeneous media. We split the domain $\Omega = (-1155 \text{ m}, 1155 \text{ m}) \times (0 \text{ m}, 2310 \text{ m})$ into two vertical layers. The left layer is characterized by the same thermoelastic properties of the test case *Shear source term*, while in the right layer, we consider the following: cf. Table 8 (the parameters that are not listed there are taken as in Table 7). This final test case aims to investigate how the heterogeneity of the media can affect the wave propagation phenomena. The forcing terms, and discretizations parameters are the same of *Shear source term*-test case.

Coefficient	Value	Coefficient	Value
μ [Pa]	10^9	λ [Pa]	$6.5 \cdot 10^8$
a_0 [Pa K ⁻²]	20	Θ [m ² Pa K ⁻² s ⁻¹]	5 I
τ_1 [s]	$2.5 \cdot 10^{-7}$	τ_2 [s]	$2.5 \cdot 10^{-7}$

Table 8: Wave propagation in thermoelastic media: heterogeneous media properties (right layer). The thermoelastic properties of the left layer are reported in Table 7.

In terms of the velocity field – displayed in Figure 15 and Figure 16 – the main difference with respect to the homogeneous case is the presence of the head waves that connect the wavefronts of the

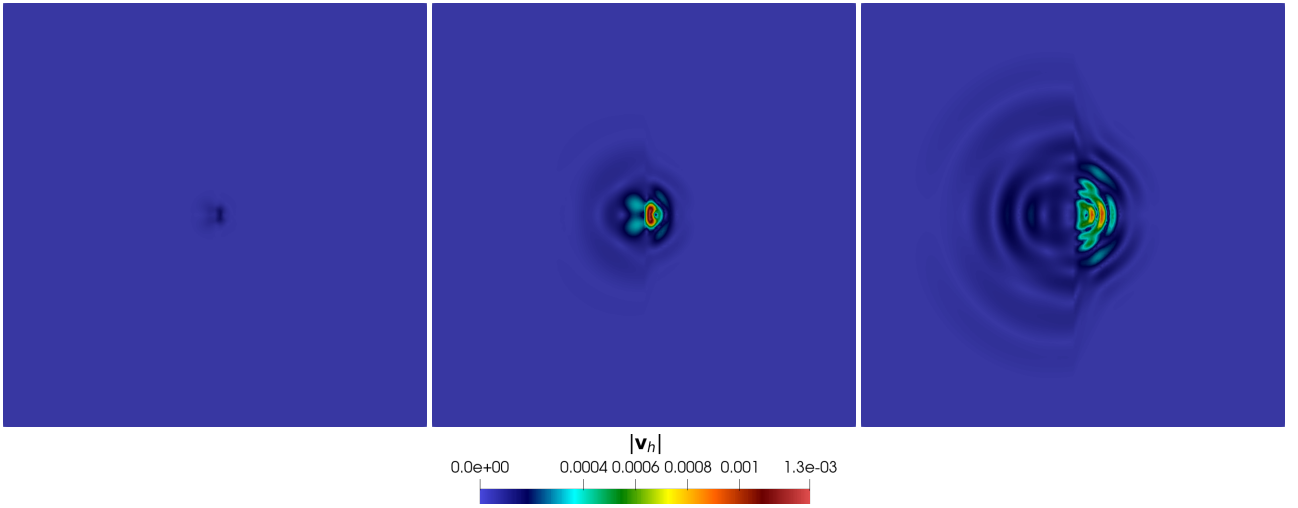


Figure 15: Wave propagation in thermoelastic media with shear source term: computed velocity field $|\mathbf{v}_h|$ at the time instants $t = 0.1\text{s}$ (left), $t = 0.3\text{s}$ (center), $t = 0.5\text{s}$ (right)

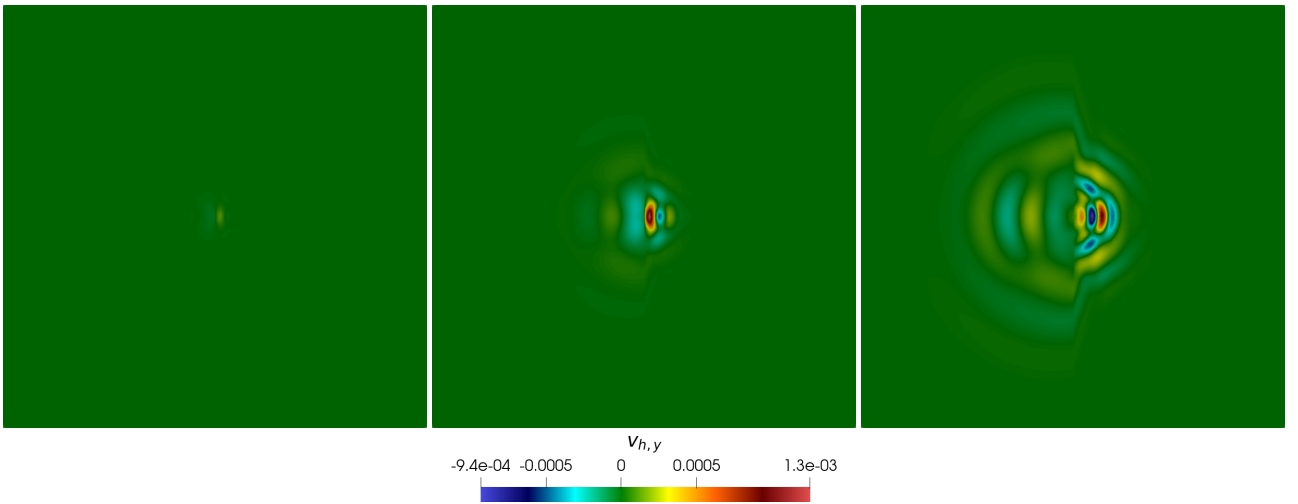


Figure 16: Wave propagation in thermoelastic media with shear source term: computed vertical component of the velocity field $v_{h,y}$ at the time instants $t = 0.1\text{s}$ (left), $t = 0.3\text{s}$ (center), $t = 0.5\text{s}$ (right).

two sub-domains. The head waves are particularly evident by looking at the vertical component of the velocity field (cf. last frame of Figure 16). For what concerns the temperature field T_h , whose behavior is shown in Figure 17, we observe how the increasing value in the thermal conductivity affects the profile of the T -wave and, even in this case, we can observe the presence of wavelets that connect the wavefronts in the two layers. In general, by looking at the results for all three fields, we can observe that the heterogeneities in the media properties are well resolved by our method and that all the symmetric and anti-symmetric patterns observed in the *Shear source term*-test case are preserved. However, the wave propagation in the two sub-layers is non-identical due to the different physical properties of the two media. We can observe a qualitatively good agreement with the results presented in [28] for the thermoelastic wave propagation and in [18, 27] for the thermo-poroelastic wave propagation.

5.5 Fluid flow in heterogeneous poro-viscoelastic media

In this section, we consider the injection of a fluid in a heterogeneous poro-viscoelastic medium inspired by the SPE10 benchmark [31]. This simulation aims to analyze the impact of the different possible modeling choices on the fluid flows in geophysical applications. We increase the initial permeability values by four orders to highlight the impact in high-permeable channels.

We consider as domain a horizontal slice (number 35) of the SPE10 benchmark $\Omega = (0 \text{ m}, 366 \text{ m}) \times$

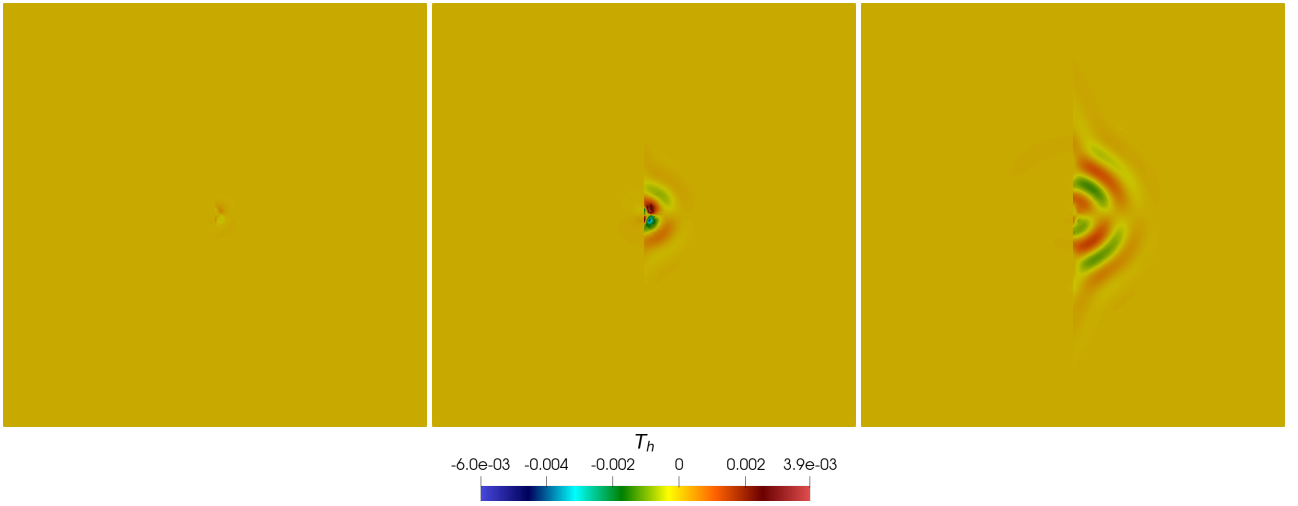


Figure 17: Wave propagation in thermoelastic media with shear source term: computed temperature field T_h at the time instants $t = 0.1s$ (left), $t = 0.3s$ (center), $t = 0.5s$ (right).

(0 m, 671 m). The permeability values associated with the simulations can be observed in Figure 18 (left). It can be observed that there is a channel of higher permeability that we expect to transport most of the fluid flow inside the domain. The simulation is associated with an injection of fluid in two sources with reabsorption in the middle of the domain. To reproduce this phenomenon, we set a forcing term:

$$g(\mathbf{x}, t) = \frac{\tanh(5t)}{10} \left(e^{-\frac{(x-190)^2+(y-550)^2}{500}} + e^{-\frac{(x-130)^2+(y-120)^2}{500}} - e^{-\frac{(x-175)^2+(y-360)^2}{500}} \right).$$

With this choice, the injection and absorption increase in time until $t = 0.5s$ when they reach a plateau. Concerning initial conditions, we set pressure, displacement, and velocity equal 0. Moreover, we set homogeneous Dirichlet boundary conditions for the displacement and homogeneous Neumann boundary conditions for the pressure. Concerning the space discretization, we use the cartesian mesh of 13200 elements provided by the SPE10 benchmark ($h = 6.81$ m). This choice lets us maintain the initial benchmark's tensor \mathbf{D} refinement level. We use the polynomial degree $\ell = 2$ and a timestep $\Delta t = 4 \times 10^{-4}$.

Parameter	Model PVE	Model P	Model D	Reference
μ [Pa]	10^9	-	-	[18]
λ [Pa]	4×10^8	-	-	[18]
δ_1 [s]	8×10^{-5}	-	-	[51]
δ_2 [s]	8×10^{-5}	-	-	[51]
γ [-]	1	0	0	[18]
d_0 [Pa $^{-1}$]	10^{-9}	10^{-9}	10^{-9}	[18]
τ_1 [s]	$\rho_f \phi^{-1} \mathbf{D}$	$\rho_f \phi^{-1} \mathbf{D}$	0	[50]
τ_2 [s]	$\rho_f \phi^{-1} \mathbf{D}$	$\rho_f \phi^{-1} \mathbf{D}$	0	[50]
ρ_f [kg m $^{-3}$]	1.025×10^3	1.025×10^3	1.025×10^3	[41]
ϕ [-]	0.1	0.1	0.1	[50]

Table 9: Fluid flow in heterogeneous poro-viscoelastic medium: physical parameters in the three simulation settings.

Starting from this general setting, which is common to all the simulations in this subsection, we construct three different models. In particular, we compare the proposed poro-viscoelastic model (PVE) with two porous media models: the first comprehensive of the acceleration term of the Darcy

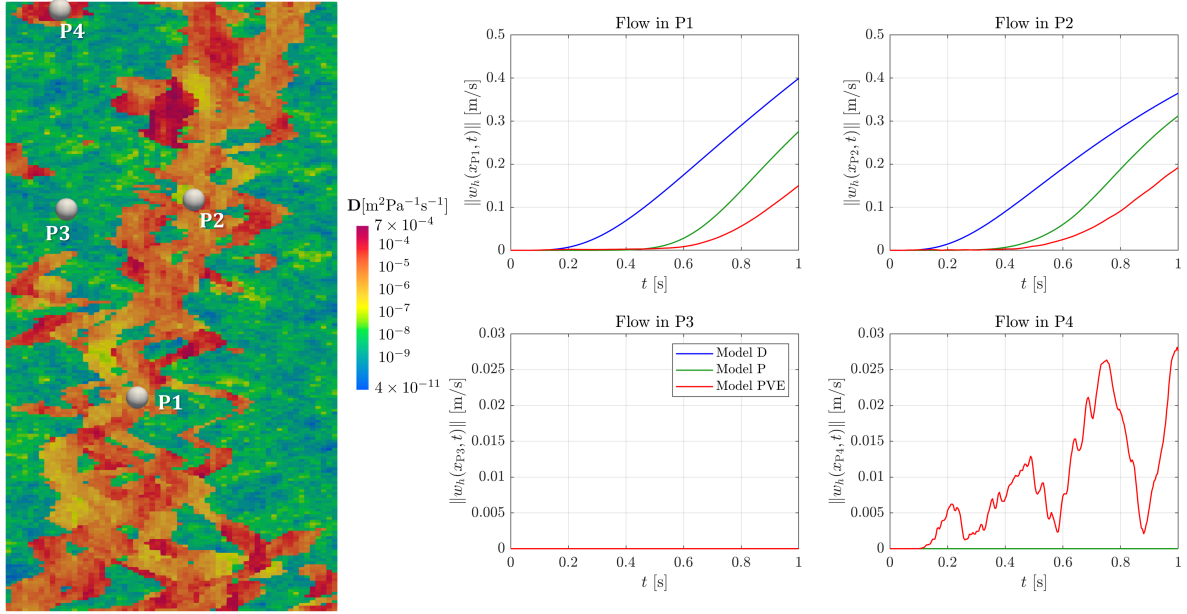


Figure 18: Fluid flow in heterogeneous porous-viscoelastic medium: computed filtration velocity field $\|\mathbf{w}_h\|$ measured in specific points of the domain with the three different models.

law (model P) and the second with a classical static Darcy law (model D). All these models can be obtained in our general framework by taking different values of the physical parameters. The values used in this simulation with the specific references are reported in Table 9.

In Figure 18, we report the result of the three models regarding the magnitude of the fluid filtration $\|\mathbf{w}_h\| = \|\mathbf{D}\nabla p_h\|$. In particular, we report the values measured in four specific points inside the domain. Concerning points P1= (146.30 m, 236.22 m) and P2= (207.26 m, 452.63 m), we can notice that the magnitude increases faster in model D than in the others. This is coherent with the modeling of the Darcy law, which does not consider fluid acceleration. This choice penalizes the fluid flow's continuity, reducing the previous timesteps' effect on the flow. Observing the model PVE, we highlight that the viscoelasticity reduces the magnitude of the flow in points P1 and P2, creating an additional delay in the fluid flow development. Concerning point P3= (67.05 m, 441.69 m), where the permeability is lower than in the other recording points, the fluid flow is approximately null in all the models (in the PVE model, the values are $\simeq 10^{-6}$ m/s). Finally, in P4= (60.96 m, 661.42 m), the elastic deformation of the soil induces a fluid flow in the model PVE, although the area is quite far from the channel in which the fluid injection is modeled.

In Figure 19, we report the complete fluid filtration field at three-time instants ($t = 0.2, 0.5, 1.0$ s) and for the three different models. In particular, the glyphs are not reported wherever the flow is null. We can observe that the gap between models PVE and P against model D reduces during the simulation after a significant distance at the first times ($t = 0.2$ s). In all the cases, the fluid flow is located along the high-permeability channel inside the domain. However, a significant difference is fluid flow induction inside non-connected high-permeability regions in model PVE, which increases over time.

To quantify the differences between the modeling choices, we construct a relative measure of filtration distance. Indeed, considering the models $*$ and $'$, we introduce for each mesh element K :

$$\|\mathbf{w}_h^* - \mathbf{w}_h'\|_r = \frac{\|\mathbf{w}_h^* - \mathbf{w}_h'\|_K}{\|\mathbf{w}_h^D\|},$$

where the choice of rescaling with $\|\mathbf{w}_h^D\|$ is guided by the fact this is the *state-of-the-art* model in literature. In Figure 20 (on the right), we report the relative differences in flow magnitude between the three models. As we can observe at time $t = 0.5$ s, in points with high permeability values, the Darcy model overestimates the flow by more than 100%. In Figure 20 (on the left), we report the mean in space (with confidence bounds computed with the standard deviation) for each time. We

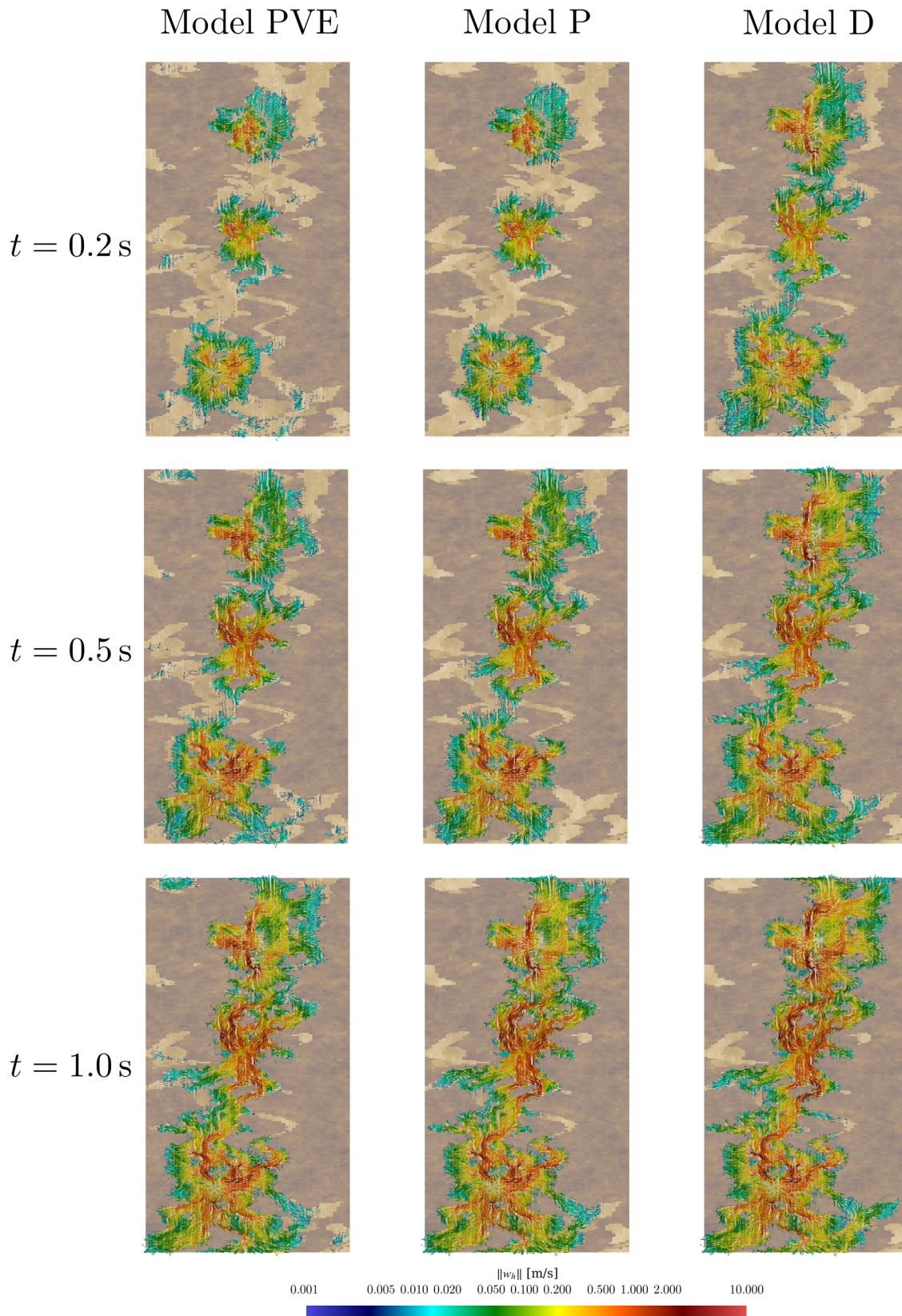


Figure 19: Fluid flow in heterogeneous porous-viscoelastic medium: computed filtration velocity field $\|\mathbf{w}_h\|$ at the time instants $t = 0.2 \text{ s}$ (top), $t = 0.5 \text{ s}$ (middle), and $t = 1.0 \text{ s}$ (bottom). Glyphs are not present wherever the flow is absent. Three different models are reported: model PVE (left), model P (middle), and model D (right).

can observe that the difference between D and P, as well as between D and PVE, decreases in time. This is coherent with the additional inertia introduced by the terms τ_1 and τ_2 . On the contrary, the

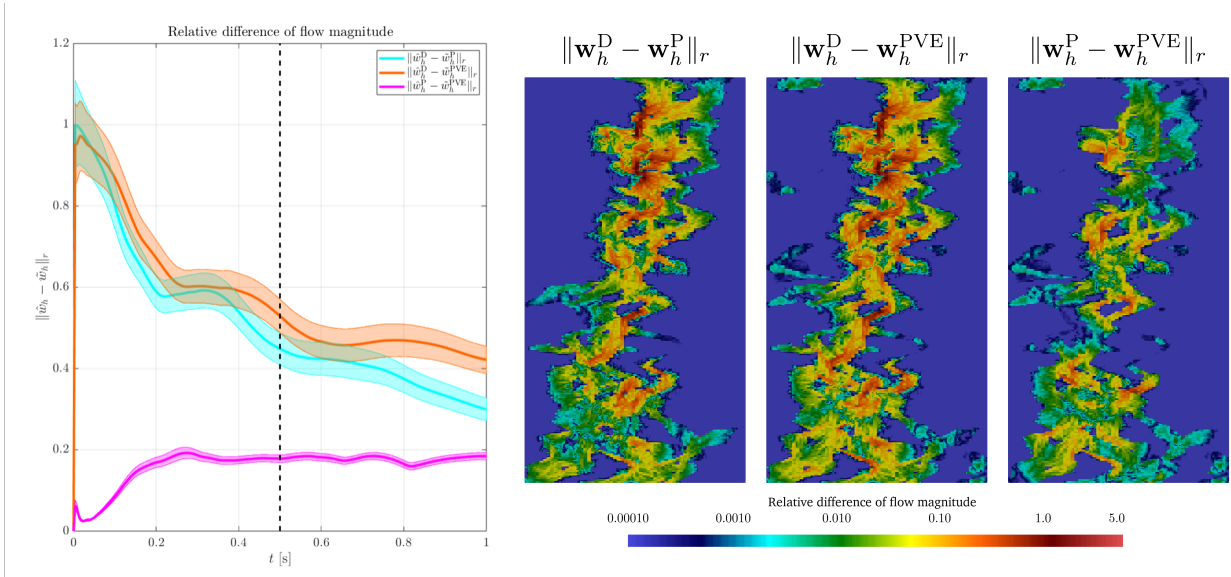


Figure 20: Relative difference of flow magnitude: mean values and confidence bounds for each time (left) and detailed differences at time 0.5 s.

difference between P and PVE is smaller than the others and almost constant in time. Indeed, after an initial time, when the models provide almost the same solution, the difference is highly guided by the capability of PVE to catch the flow in high permeability regions detached from the central channel. Finally, we underline that neglecting components of the mathematical model in choosing the Darcy law can sensibly affect the final solution.

6 Conclusions

In this work, we have presented a PolyDG formulation for the thermo/poro-viscoelasticity problem. The model derivation remarks on which terms are more or less significant depending on the physical parameters of our test cases and, consequently, on the reference application. The stability estimate in the semi-discrete framework highlights the mild requirements on the physical parameters of the model problem. Moreover, it is general with respect to the choice of a fully-inertial or quasi-static model. Numerical simulations are performed to test the convergence and robustness properties of the proposed method. The results also show that the method provides a good approximation when considering limit cases in the ranges of physical parameters and presents some partial-superconvergence results. Finally, some benchmark verifications and physically sound test cases are presented, showing that the PolyDG discretization scheme can be appealing for real problem simulations with appropriate parameters. In particular, we used the Spe10 benchmark to highlight the impact of modeling choice on the fluid flow in heterogeneous media in geophysics.

Further developments of the present work are possible. In particular, we mention the extension to other non-linear models for visco-elasticity. Secondly, to reduce the large computational cost required to deal with the fully coupled problem, two possible approaches are designing effective preconditioning techniques for the resulting system and developing effective splitting schemes. Given the improvements in the linear system resolution strategy, extending the implementation to the three-dimensional case is a further possible improvement. For this, generating and managing the computational mesh is also a point of development and interest.

Acknowledgements

We acknowledge Paola F. Antonietti and Michele Botti (MOX - Dipartimento di Matematica, Politecnico di Milano, Italy) for the helpful discussions. MC has been funded from the European Union (ERC SyG, NEMESIS, project number 101115663). Views and opinions expressed are however those

of the authors only and do not necessarily reflect those of the European Union or the European Research Council Executive Agency. Neither the European Union nor the granting authority can be held responsible for them. SB has been funded by the research grant PRIN2020 n. 20204LN5N5 funded by the Italian Ministry of Universities and Research (MUR). SB and MC are members of INdAM-GNCS. The present research is part of the activities of the project Dipartimento di Eccellenza 2023-2027, Dipartimento di Matematica, Politecnico di Milano.

References

- [1] P. F. Antonietti, S. Giani, and P. Houston. *hp*-version composite discontinuous Galerkin methods for elliptic problems on complicated domains. *SIAM J. Sci. Comput.*, 35(3):A1417–A1439, 2013.
- [2] P. F. Antonietti, M. Botti, I. Mazzieri, and S. Nati Poltri. A high-order discontinuous Galerkin method for the poro-elasto-acoustic problem on polygonal and polyhedral grids. *SIAM J. Sci. Comput.*, 44(1):B1–B28, 2021.
- [3] P. F. Antonietti, M. Botti, and I. Mazzieri. On mathematical and numerical modelling of multiphysics wave propagation with polytopal discontinuous Galerkin methods: a review. *Vietnam Journal of Mathematics*, 2022.
- [4] P. F. Antonietti, S. Bonetti, and M. Botti. Discontinuous Galerkin approximation of the fully coupled thermo-poroelastic problem. *SIAM J. Sci. Comput.*, 45(2):A621–A645, 2023.
- [5] P. F. Antonietti, S. Bonetti, M. Botti, M. Corti, I. Fumagalli, and I. Mazzieri. **lymph**: discontinuous poLYtopal methods for Multi-PHYsics differential problems. *arXiv preprint arXiv:2401.13376*, 2024.
- [6] D. N. Arnold. An interior penalty finite element method with discontinuous elements. *SIAM J. Numer. Anal.*, 19(4):742–760, 1982.
- [7] D. N. Arnold, F. Brezzi, B. Cockburn, and L. D. Marini. Unified analysis of discontinuous Galerkin methods for elliptic problems. *SIAM J. Numer. Anal.*, 39(5):1749–1779, 2002.
- [8] R. Asadi and B. Ataie-Ashtiani. Hybrid finite volume-finite element methods for hydro-mechanical analysis in highly heterogeneous porous media. *Comput. Geotech.*, 132:103996, 2021.
- [9] S. Bajpai, D. Goswami, and K. Ray. Fully discrete finite element error analysis of a discontinuous Galerkin method for the Kelvin-Voigt viscoelastic fluid model. *Comput. Math. Appl.*, 130:69–97, 2023.
- [10] L. Barden. Primary and secondary consolidation of clay and peat. *Géotechnique*, 18(1):1–24, 1968.
- [11] R. L. Berge, I. Berre, E. Keilegavlen, J. M. Nordbotten, and B. Wohlmuth. Finite volume discretization for poroelastic media with fractures modeled by contact mechanics. *Int. J. Numer. Methods Eng.*, 121(4):644–663, 2020.
- [12] M. A. Biot. General theory of three dimensional consolidation. *J. Appl. Phys.*, 12(2):155–164, 1941.
- [13] L. Bociu, G. Guidoboni, R. Sacco, and J. T. Webster. Analysis of nonlinear poro-elastic and poro-visco-elastic models. *Arch. Ration. Mech. Anal.*, 222(3):1445–1519, 2016.
- [14] L. Bociu, G. Guidoboni, R. Sacco, and M. Verri. On the role of compressibility in poroviscoelastic models. *Math. Biosci. Eng.*, 16(5):6167–6208, 2019.
- [15] L. Bociu, S. Canic, B. Muha, and J. T. Webster. Multilayered poroelasticity interacting with Stokes flow. *SIAM J. Math. Anal.*, 53(6):6243–6279, 2021.

- [16] L. Bociu, B. Muha, and J. T. Webster. Weak solutions in nonlinear poroelasticity with incompressible constituents. *Nonlinear Anal. Real World Appl.*, 67:103563, 2022.
- [17] L. Bociu, B. Muha, and J. T. Webster. Mathematical effects of linear visco-elasticity in quasi-static Biot models. *J. Math. Anal. Appl.*, 527(2):127462, 2023.
- [18] S. Bonetti, M. Botti, I. Mazzieri, and P. F. Antonietti. Numerical modeling of wave propagation phenomena in thermo-poroelastic media via discontinuous Galerkin methods. *J. Comput. Phys.*, 489:112275, 2023.
- [19] S. Bonetti, M. Botti, and P. F. Antonietti. Robust discontinuous Galerkin-based scheme for the fully-coupled nonlinear thermo-hydro-mechanical problem. *IMA J. Numer. Anal.*, page drae045, 2024.
- [20] J. W. Both, M. Borregales, J. M. Nordbotten, K. Kumar, and F. A. Radu. Robust fixed stress splitting for Biot’s equations in heterogeneous media. *Appl. Math. Lett.*, 68:101–108, 2017.
- [21] M. Botti, D. A. Di Pietro, and P. Sochala. A hybrid high-order discretization method for nonlinear poroelasticity. *Comput. Methods Appl. Math.*, 20(2):227–249, 2020.
- [22] A. Boukamel, S. Méo, O. Débordes, and M. Jaeger. A thermo-viscoelastic model for elastomeric behaviour and its numerical application. *Arch. Appl. Mech.*, 71(12):785–801, 2001.
- [23] M. K. Brun, I. Berre, J. M. Nordbotten, and F. A. Radu. Upscaling of the coupling of hydromechanical and thermal processes in a quasi-static poroelastic medium. *Transp. Porous Media*, 124(1):137–158, 2018.
- [24] M. K. Brun, E. Ahmed, J. M. Nordbotten, and F. A. Radu. Well-posedness of the fully coupled quasi-static thermo-poroelastic equations with nonlinear convective transport. *J. Math. Anal. Appl.*, 471(1):239–266, 2019.
- [25] A. Cangiani, E. H. Georgoulis, and P. Houston. hp-version discontinuous Galerkin methods on polygonal and polyhedral meshes. *Math. Models Methods Appl. Sci.*, 24(10):2009–2041, 2014.
- [26] A. Cangiani, Z. Dong, E. H. Georgoulis, and P. Houston. *hp-version discontinuous Galerkin methods on polytopic meshes*. SpringerBriefs in Mathematics. Springer International Publishing, 2017.
- [27] J. M. Carcione, F. Cavallini, E. Wang, J. Ba, and L.-Y. Fu. Physics and simulation of wave propagation in linear thermoporoelastic media. *J. Geophys. Res. Solid Earth*, 124(8):8147–8166, 2019.
- [28] J. M. Carcione, Z.-W. Wang, W. Ling, E. Salusti, J. Ba, and L.-Y. Fu. Simulation of wave propagation in linear thermoelastic media. *Geophysics*, 84(1):T1–T11, 2019.
- [29] N. Castelletto, S. Klevtsov, H. Hajibeygi, and H. A. Tchelepi. Multiscale two-stage solver for Biot’s poroelasticity equations in subsurface media. *Comput. Geosci.*, 23(2):207–224, 2019.
- [30] M. Causemann, V. Vinje, and M. E. Rognes. Human intracranial pulsatility during the cardiac cycle: a computational modelling framework. *Fluids Barriers CNS*, 19(1):84, 2022.
- [31] M. A. Christie and M. J. Blunt. Tenth SPE comparative solution project: A comparison of upscaling techniques. *SPE Reservoir Evaluation & Engineering*, 4(04):308–317, 2001. doi: 10.2118/72469-PA.
- [32] M. Corti, P. F. Antonietti, L. Dede’, and A. M. Quarteroni. Numerical modeling of the brain poromechanics by high-order discontinuous Galerkin methods. *Math. Models Methods Appl. Sci.*, 33(08):1577–1609, 2023.
- [33] O. Coussy. *Thermoporoelasticity*, chapter 4, pages 71–112. John Wiley & Sons, Ltd, 2003.

- [34] J. de la Puente, M. Dumbser, M. Käser, and H. Igel. Discontinuous Galerkin methods for wave propagation in poroelastic media. *Geophysics*, 73(5):T77–T97, 2008.
- [35] E. Detournay and A. H.-D. Cheng. 5 - Fundamentals of poroelasticity. In *Analysis and Design Methods*, pages 113–171. Pergamon, 1993.
- [36] D. A. Di Pietro and J. Droniou. *The Hybrid High-Order Method for Polytopal Meshes: Design, Analysis, and Applications*. Springer, 2020. doi: doi.org/10.1007/978-3-030-37203-3.
- [37] G. Duvaut and J. L. Lions. *Inequalities in Mechanics and Physics*. Springer, 219 edition, 1976.
- [38] A. Ern, A. F. Stephansen, and P. Zunino. A discontinuous Galerkin method with weighted averages for advection–diffusion equations with locally small and anisotropic diffusivity. *IMA Journal of Numerical Analysis*, 29(2):235–256, 2009.
- [39] B. Flemisch, I. Berre, W. Boon, A. Fumagalli, N. Schwenck, A. Scotti, I. Stefansson, and A. Tatomir. Benchmarks for single-phase flow in fractured porous media. *Adv. Water Resour.*, 111:239–258, 2018.
- [40] G. Fu. A high-order HDG method for the Biot’s consolidation model. *Comput. Math. Appl.*, 77(1):237–252, 2019.
- [41] A. Fumagalli and F. Patacchini. Numerical validation of an adaptive model for the determination of nonlinear-flow regions in highly heterogeneous porous media, 2024.
- [42] F. Gaspar, J. Gracia, F. Lisbona, and P. Vabishchevich. A stabilized method for a secondary consolidation Biot’s model. *Numer. Methods Partial Differ. Equ.*, 24(1):60–78, 2008.
- [43] B. Heinrich and K. Pietsch. Nitsche type mortaring for some elliptic problem with corner singularities. *Computing*, 68(3):217–238, 2002.
- [44] A. Jafari, P. Broumand, M. Vahab, and N. Khalili. An eXtended finite element method implementation in COMSOL multiphysics: Solid mechanics. *Finite Elem. Anal. Des.*, 202:103707, 2022.
- [45] C. Kreuzer and P. Zanotti. Inf-sup stable discretization of the quasi-static biot’s equations in poroelasticity. *arXiv*, 2024.
- [46] J. J. Lee, E. Piersanti, K.-A. Mardal, and M. E. Rognes. A mixed finite element method for nearly incompressible multiple-network poroelasticity. *SIAM J. Sci. Comput.*, 41(2):A722–A747, 2019.
- [47] C. Morency and J. Tromp. Spectral-element simulations of wave propagation in porous media. *Geophys. J. Int.*, 175(1):301–345, 2008.
- [48] V. C. Mow, S. C. Kuei, W. M. Lai, and C. G. Armstrong. Biphasic creep and stress relaxation of articular cartilage in compression: Theory and experiments. *J. Biomech. Eng.*, 102(1):73–84, 1980.
- [49] M. A. Murad and J. H. Cushman. Multiscale flow and deformation in hydrophilic swelling porous media. *Int. J. Eng. Sci.*, 34(3):313–338, 1996.
- [50] D. A. Nield and A. Bejan. *Convection in Porous Media*. Springer International Publishing, 5 edition, 2017.
- [51] M. S. Proença, A. T. Paschoalini, J. B. C. Silva, A. Souza, D. H. S. Obata, L. P. M. Lima, and O. D. Z. Boaventura. The finite element method applied in the viscoelastic constitutive model of Kelvin–Voigt for characterization of the soil dynamic response to water leakage simulation. *J. Braz. Soc. Mech. Sci. Eng.*, 44:470, 2022.

- [52] A. Quarteroni. *Numerical Models for Differential Problems*. Springer, 3 edition, 2017.
- [53] C. Rodrigo, F. Gaspar, X. Hu, and L. Zikatanov. Stability and monotonicity for some discretizations of the Biot’s consolidation model. *Comput. Methods Appl. Mech. Eng.*, 298:183–204, 2016.
- [54] E. Rohan, S. Shaw, M. F. Wheeler, and J. R. Whiteman. Mixed and Galerkin finite element approximation of flow in a linear viscoelastic porous medium. *Comput. Methods Appl. Mech. Eng.*, 260:78–91, 2013.
- [55] T. F. Russell and M. F. Wheeler. *2. Finite Element and Finite Difference Methods for Continuous Flows in Porous Media*, pages 35–106. Society for Industrial and Applied Mathematics, 1983.
- [56] E. Sanchez-Palencia. *Non-Homogeneous Media and Vibration Theory*. Lecture Notes in Physics. Springer Berlin Heidelberg, 1980.
- [57] M. Schneider, L. Agélas, G. Enchéry, and B. Flemisch. Convergence of nonlinear finite volume schemes for heterogeneous anisotropic diffusion on general meshes. *J. Comput. Phys.*, 351:80–107, 2017.
- [58] R. Showalter. Diffusion in poro-elastic media. *J. Math. Anal. Appl.*, 251(1):310–340, 2000.
- [59] M. F. Souzañchi, L. Cardoso, and S. C. Cowin. Tortuosity and the averaging of microvelocity fields in poroelasticity. *J. Appl. Mech.*, 80(2), 2013. 020906.
- [60] I. Stefansson, I. Berre, and E. Keilegavlen. A fully coupled numerical model of thermo-hydro-mechanical processes and fracture contact mechanics in porous media. *Comput. Methods Appl. Mech. Eng.*, 386:114122, 2021.
- [61] R. Stenberg. Mortaring by a method of J.A. Nitsche. *Computational mechanics*, 1998.
- [62] K. Terzaghi. *Theoretical soil mechanics*. John Wiley & Sons, Ltd, 1943.
- [63] C. J. van Duijn and A. Mikelić. Mathematical theory of nonlinear single-phase poroelasticity. *J. Nonlinear Sci.*, 33(3):44, 2023.
- [64] M. F. Wheeler. An elliptic collocation-finite element method with interior penalties. *SIAM J. Numer. Anal.*, 15(1):152–161, 1978.

A Derivation of Newmark- β - θ method

In this appendix, we show the computations to derive the Newmark- β - θ method for discretizing the equations with $\tau_1 = 0$. We use the Newmark- β method for the first equation of (8). To this aim, we introduce the velocity vector $\mathbf{Z} = \dot{\mathbf{U}}$ and the acceleration vector $\mathbf{A} = \ddot{\mathbf{U}}$. Then, at each time-step t^n , we solve the following set of equations:

$$\left\{ \begin{array}{l} \left(\frac{1}{\beta_N \Delta t^2} \mathbf{M}_u + \mathbf{A}_e + \mathbf{A}_{\text{div}} \right) \mathbf{U}^{n+1} + (\mathbf{A}_{e,\delta_1} + \mathbf{A}_{\text{div},\delta_2}) \mathbf{Z}^{n+1} - \mathbf{C}^T \boldsymbol{\Phi}^{n+1} = \mathbf{F}^{n+1} + \frac{1}{\beta_N \Delta t^2} \mathbf{M}_u \mathbf{U}^n \\ \quad + \frac{1}{\beta_N \Delta t} \mathbf{M}_u \mathbf{Z}^n + \frac{1-2\beta_N}{2\beta_N} \mathbf{M}_u \mathbf{A}^n, \\ \mathbf{Z}^{n+1} = \mathbf{Z}^n + \Delta t (\gamma_N \mathbf{A}^{n+1} + (1-\gamma_N) \mathbf{A}^n), \\ \mathbf{A}^{n+1} = \frac{1}{\beta_N \Delta t^2} (\mathbf{U}^{n+1} - \mathbf{U}^n) - \frac{1}{\beta_N \Delta t} \mathbf{Z}^n + \frac{2\beta_N - 1}{2\beta_N} \mathbf{A}^n. \end{array} \right. \quad (11)$$

In the first equation of (11) we can plug the expressions for \mathbf{Z}^{n+1} , \mathbf{A}^{n+1} to get:

$$\left(\frac{1}{\beta_N \Delta t^2} \mathbf{M}_u + \mathbf{A}_u + \frac{\gamma_N}{\beta_N \Delta t} \mathbf{A}_{u,\delta} \right) \mathbf{U}^{n+1} - \mathbf{C}^T \boldsymbol{\Phi}^{n+1} = \mathbf{F}^{n+1} + \left(\frac{1}{\beta_N \Delta t^2} \mathbf{M}_u + \frac{\gamma_N}{\beta_N \Delta t} \mathbf{A}_{u,\delta} \right) \mathbf{U}^n \\ + \left(\frac{1}{\beta_N \Delta t} \mathbf{M}_u - \frac{\beta_N - \gamma_N}{\beta_N} \mathbf{A}_{u,\delta} \right) \mathbf{Z}^n + \left(\frac{1-2\beta_N}{2\beta_N} \mathbf{M}_u - \frac{\Delta t(2\beta_N - \gamma_N)}{2\beta_N} \mathbf{A}_{u,\delta} \right) \mathbf{A}^n,$$

where, for the sake of clarity, we have introduced the notation $\mathbf{A}_u = \mathbf{A}_e + \mathbf{A}_{\text{div}}$, $\mathbf{A}_{u,\delta} = \mathbf{A}_{e,\delta_1} + \mathbf{A}_{\text{div},\delta_2}$. Then, we couple (11) with a θ -method for the pressure equation. To obtain the formulation, we plug into the second equation in (8) the definition of the velocity \mathbf{Z} and of the acceleration \mathbf{A} at time-continuous level. Thus, we get the following expression:

$$\mathbf{M}_\varphi \dot{\Phi}(t) + \mathbf{C}_{\tau_2} \mathbf{A}(t) + \mathbf{C} \mathbf{Z}(t) + \mathbf{A}_\varphi \Phi(t) = \mathbf{G}(t), \quad t \in (0, T_f].$$

Using this form of the pressure equation, the discretized equation reads:

$$\begin{aligned} \left(\frac{1}{\Delta t} \mathbf{M}_\varphi + \theta \mathbf{A}_\varphi \right) \Phi^{n+1} + \theta (\mathbf{C}_{\tau_2} \mathbf{A}^{n+1} + \mathbf{C} \mathbf{Z}^{n+1}) &= \left(\frac{1}{\Delta t} \mathbf{M}_\varphi - (1 - \theta) \mathbf{A}_\varphi \right) \Phi^n + \theta \mathbf{G}^{n+1} \\ + (1 - \theta) (\mathbf{G}^n - \mathbf{C}_{\tau_2} \mathbf{A}^n - \mathbf{C} \mathbf{Z}^n) \end{aligned}$$

and by using the expressions for \mathbf{Z}^{n+1} , \mathbf{A}^{n+1} in (11) we obtain:

$$\begin{aligned} \left(\frac{1}{\Delta t} \mathbf{M}_\varphi + \theta \mathbf{A}_\varphi \right) \Phi^{n+1} + \mathbf{C}_u \mathbf{U}^{n+1} &= \theta \mathbf{G}^{n+1} + \tilde{\theta} \mathbf{G}^n + \left(\frac{1}{\Delta t} \mathbf{M}_\varphi - \tilde{\theta} \mathbf{A}_\varphi \right) \Phi^n \\ + \mathbf{C}_u \mathbf{U}^n + \mathbf{C}_z \mathbf{Z}^n + \mathbf{C}_a \mathbf{A}^n, \end{aligned}$$

where:

$$\begin{aligned} \mathbf{C}_u &= \frac{\theta}{\beta_N \Delta t^2} (\mathbf{C}_{\tau_2} + \Delta t \gamma \mathbf{C}), \\ \mathbf{C}_z &= \left(\frac{\theta}{\beta_N \Delta t} \mathbf{C}_{\tau_2} + \frac{\theta \gamma_N - \beta_N}{\beta_N} \mathbf{C} \right), \\ \mathbf{C}_a &= \left(\frac{\theta - 2\beta_N}{2\beta_N} \mathbf{C}_{\tau_2} + \frac{\theta \Delta t (\gamma - 2\beta_N)}{2\beta_N} \mathbf{C} \right), \end{aligned}$$

and $\tilde{\theta} = 1 - \theta$. Thus, the final algebraic discretized formulation reads:

$$\left\{ \begin{aligned} &\left(\frac{1}{\beta_N \Delta t^2} \mathbf{M}_u + \mathbf{A}_u + \frac{\gamma_N}{\beta_N \Delta t} \mathbf{A}_{u,\delta} \right) \mathbf{U}^{n+1} - \mathbf{C}^T \Phi^{n+1} = \mathbf{F}^{n+1} + \left(\frac{1}{\beta_N \Delta t^2} \mathbf{M}_u + \frac{\gamma_N}{\beta_N \Delta t} \mathbf{A}_{u,\delta} \right) \mathbf{U}^n \\ &\quad + \left(\frac{1}{\beta_N \Delta t} \mathbf{M}_u - \frac{\beta_N - \gamma_N}{\beta_N} \mathbf{A}_{u,\delta} \right) \mathbf{Z}^n + \left(\frac{1 - 2\beta_N}{2\beta_N} \mathbf{M}_u - \frac{\Delta t (2\beta_N - \gamma_N)}{2\beta_N} \mathbf{A}_{u,\delta} \right) \mathbf{A}^n, \\ &\left(\frac{1}{\Delta t} \mathbf{M}_\varphi + \theta \mathbf{A}_\varphi \right) \Phi^{n+1} + \mathbf{C}_u \mathbf{U}^{n+1} = \theta \mathbf{G}^{n+1} + \tilde{\theta} \mathbf{G}^n + \left(\frac{1}{\Delta t} \mathbf{M}_\varphi - \tilde{\theta} \mathbf{A}_\varphi \right) \Phi^n \\ &\quad + \mathbf{C}_u \mathbf{U}^n + \mathbf{C}_z \mathbf{Z}^n + \mathbf{C}_a \mathbf{A}^n, \\ &\mathbf{Z}^{n+1} = \mathbf{Z}^n + \Delta t (\gamma_N \mathbf{A}^{n+1} + (1 - \gamma_N) \mathbf{A}^n), \\ &\mathbf{A}^{n+1} = \frac{1}{\beta_N \Delta t^2} (\mathbf{U}^{n+1} - \mathbf{U}^n) - \frac{1}{\beta_N \Delta t} \mathbf{Z}^n + \frac{2\beta_N - 1}{2\beta_N} \mathbf{A}^n, \end{aligned} \right.$$